bioRxiv preprint doi: https://doi.org/10.1101/114876; this version posted March 7, 2017. The copyright holder for this preprint (which was not certified by peer review) is the author/funder. All rights reserved. No reuse allowed without permission.

SPOT DYNAMICS IN A REACTION-DIFFUSION MODEL OF PLANT ROOT HAIR INITIATION

DANIELE AVITABILE *, VICTOR F. BREÑA–MEDINA †, AND MICHAEL J. WARD ‡

Abstract. We study pattern formation aspects in a 2-D reaction-diffusion (RD) sub-cellular model characterizing the effect of a spatial gradient of a plant hormone distribution on a family of G-proteins associated with root-hair (RH) initiation in the plant cell *Arabidopsis thaliana*. The activation of these G-proteins, known as the Rho of Plants (ROPs), by the plant hormone auxin, is known to promote certain protuberances on root hair cells, which are crucial for both anchorage and the uptake of nutrients from the soil. Our mathematical model for the activation of ROPs by the auxin gradient is an extension of the model proposed by Payne and Grierson [PLoS ONE, **12**(4), (2009)], and consists of a two-component generalized Schnakenberg RD system with spatially heterogeneous coefficients on a 2-D domain. The nonlinear kinetics in this RD system model the nonlinear interactions between the active and inactive forms of ROPs. By using a singular perturbation analysis to study 2-D localized spatial patterns of active ROPs, it is shown that the spatial variations in certain nonlinear terms in the reaction kinetics, due to the auxin gradient, lead to a slow spatial alignment of the localized regions of active ROPs along the longitudinal midline of the plant cell. Numerical bifurcation analysis, together with time-dependent numerical simulations of the RD system are used to illustrate 2-D localized patterns in the model, as well as the spatial alignment of localized structures.

1. Introduction. We examine the effect of a spatially-dependent plant hormone distribution on a family of proteins associated with root hair (RH) initiation in a specific plant cell. This process is modeled by a generalized Schnakenberg reaction-diffusion (RD) system on a 2-D domain with both source and loss terms, and with a spatial gradient modeling the spatially inhomogeneous distribution of plant hormone. This system is an extension of a model proposed by Payne and Grierson in [28], and analyzed in a 1-D context in the companion articles [4, 6].

In this model, an on-and-off switching process of a small G-protein subfamily, called the Rho of Plants (ROPs), is assumed to occur in a RH cell of the plant *Arabidopsis thaliana*. ROPs are known to be involved in RH cell morphogenesis at several distinct stages (see [10, 19, 27] for details). Such a biochemical process is believed to be catalyzed by a plant hormone called auxin (cf. [28]). Typically, auxin-transport models are formulated to study polarization events between cells (cf. [11]). However, little is known about specific details of auxin flow within a cell. In [4, 6, 28] a simple transport process is assumed to govern the auxin flux through a RH cell, which postulates that auxin diffuses much faster than ROPs in the cell, owing partially to the in- and out-pump mechanism that injects auxin into RH cells from both RH and non-RH cells (cf. [3, 13, 15]). Recently, in [24], a model based on the one proposed in [28] has been used to describe patch location of ROP GTPases activation along a 2-D root epidermal cell plasma membrane. This model is formulated as a two-stage process, one for ROP dynamics and another for auxin dynamics. The latter process is assumed to be described by a constant auxin production at the source together with passive diffusion and a constant auxin bulk degradation away from the source. In [24] the auxin gradient is included in the ROP finite-element

*Centre for Mathematical Medicine and Biology, School of Mathematical Sciences, University of Nottingham, University Park, Nottingham, NG7 2RD, daniele.avitabile@nottingham.ac.uk, https://www.maths.nottingham.ac.uk/personal/pmzda/.

†Centro de Ciencias Matemáticas, UNAM, Morelia, Michoacán, México, victorb@matmor.unam.mx, http://matmor.unam.mx/~victorb/.

‡Department of Mathematics, UBC, Vancouver, Canada, ward@math.ubc.ca, https://www.math.ubc.ca/~ward/.

bioRxiv preprint doi: https://doi.org/10.1101/114876; this version posted March 7, 2017. The copyright holder for this preprint (which was not certified by peer review) is the author/funder. All rights reserved. No reuse allowed without permission.

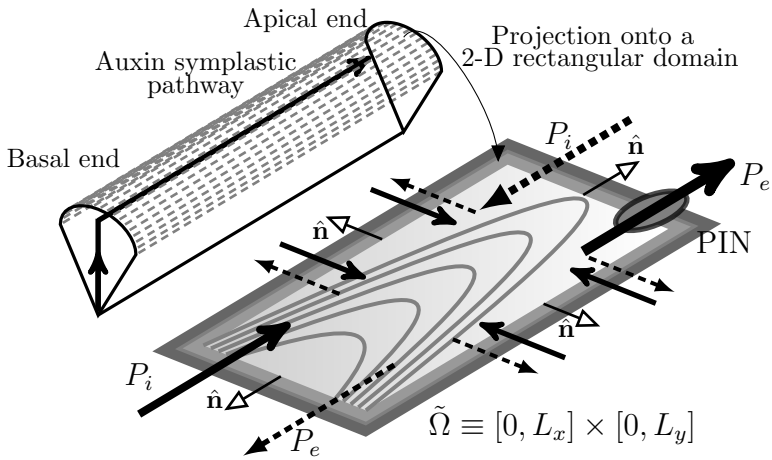

FIG. 1. *Sketch of an idealized 3-D RH cell with longitudinal and transversal spatially-dependent auxin flow. The auxin gradient is shown as a consequence of in- (solid arrows) and out-pump (dashed arrows) mechanisms. Influx P_i and efflux P_e permeabilities are respectively depicted by the direction of the arrow; the auxin symplastic pathway is indicated by black solid arrows in the 3-D RH cell. Here, the cell membrane is depicted by heavily dashed gray lines. The gradient is coloured as a light gray shade, and auxin gradient level curves are plotted in gray. Cell wall and cell membrane are coloured in dark and light gray respectively. Modified figure reproduced from [6].*

numerical simulation after a steady-state is attained. Since we are primarily interested in the biochemical interactions that promote RHs, rather than providing a detailed model of auxin transport in the cell, we shall hypothesize a specific, but qualitatively reasonable, time-independent spatially varying expression for the auxin distribution in a 2-D azimuthal projection of a 3-D RH cell wall. This modeling leads to a spatially-dependent coefficient in the RD system for ROP dyanmics. We will show that this spatial heterogeneity in the RD system induces wave-pinning effects and, ultimately, a spatial alignment of localized regions of elevated ROP concentration.

Since an RH cell is an epidermal cell, and AUX/LAX influx and PIN efflux carriers are distributed along the cell membrane, the auxin flux is known to be primarily directed from the tip of the cell towards the elongation zone (cf. [13, 17, 23]), leading to a longitudinally spatially decreasing auxin distribution. Although the auxin can follow both *apoplastic* and *symplastic* pathways, we are interested in the latter pathway which is directed within the cell and, consequently, induces the biochemical switching process. In Figure 1, a sketch of an idealized 3-D RH cell is shown. In this figure, heavily dashed gray lines represent the RH cell membrane. The auxin flux is represented by black arrows, which schematically illustrates a longitudinal decreasing symplastic pathway. In addition, a projection onto a 2-D rectangular domain of this cell is also shown in Figure 1.

In [6] we considered the 1-D version of the RD model, where the RH cell is assumed to be slim and flat. There it was shown that localized steady-state patterns, representing active-ROP proteins, slowly drift towards the interior of the domain and asymmetrically get pinned to specific spatial locations by the auxin gradient. This pinning effect, induced by the inhomogeneous auxin distribution, has been experimentally observed in [10, 12, 26]. Moreover, multiple swelling formation in transgenic RH cells may occur, though not all of these will undergo the transition to tip growth (cf. [18]). In [6] a linear stability analysis showed that multiple-active-ROP spikes

bioRxiv preprint doi: https://doi.org/10.1101/114876; this version posted March 7, 2017. The copyright holder for this preprint (which was not certified by peer review) is the author/funder. All rights reserved. No reuse allowed without permission.

may be linearly stable on $\mathcal{O}(1)$ time-scales, with the stability properties depending on an inversely proportional relationship between length and auxin catalytic strength. This dynamic phenomena can be understood as a consequence of an auxin catalytic process sustaining cell wall softening as the RH cell grows. For further discussion of this correlation between growth and biochemical catalysis see [6].

In [4] the linear stability of 1-D patterns of elevated ROP concentration to 2-D spatially transverse perturbations was analyzed. More specifically, in [4] it was shown that single interior stripes and multi-stripe patterns are ustable under small transverse perturbations. These stripes represent a particular configuration of active-ROP patches, and the loss of stability of the stripe pattern was shown to lead to more intricate patterns consisting of spots, or a boundary stripe together with multiple spots (see Fig. 9 of [4]). Moreover, it was shown that a single boundary stripe can also lose stability and lead to spot formation in the limit of small diffusivity ratio. The main goal of this paper is to study the subsequent evolution of these localized spots and, in particular, to analyze how the auxin gradient ultimately leads to a steady-state spot pattern with spots aligned with the direction of the auxin gradient.

In our RD model below, $U(\mathbf{X},T)$ and $V(\mathbf{X},T)$ denoteactive- and inactive-ROP densities, respectively, at time $T>0$ and point $\mathbf{X}=(X,Y)\in\tilde{\Omega}\subset\mathbb{R}^2$, where $\tilde{\Omega}$ is the rectangular domain $\tilde{\Omega}=[0,L_x]\times[0,L_y]$. The on-and-off switching interaction is assumed to take place on the cell membrane, which is coupled through a standard Fickian-type diffusive process for both densities (cf. [6, 28]). Although RH cells are flanked by non-RH cells (cf. [14]), there is in general no exchange of ROPs between them. Therefore, no-flux boundary conditions are assumed on $\partial\tilde{\Omega}$. We will consider two specific forms for the spatially dependent dimensionless auxin distribution α: (i) a steady monotone decreasing longitudinal gradient, which is constant in the transverse direction, and (ii) a steady monotone decreasing longitudinal gradient, which decreases on either side of the longitudinal midline $Y=L_y/2$. These two forms are modelled explicitly as

$$\text{(1.1)}\quad \text{(i) } \alpha(\mathbf{X})=\exp\left(-\frac{\nu X}{L_x}\right)\,,\quad \text{(ii) } \alpha(\mathbf{X})=\exp\left(-\frac{\nu X}{L_x}\right)\sin\left(\frac{\pi Y}{L_y}\right)\,,\quad \nu=1.5\,.$$

As formulated in [4] and [6], the basic dimensionless model consists of the two-component RD system

$$\text{(1.2a)}\qquad U_t=\varepsilon^2\Delta U+\alpha\left(\mathbf{x}\right)U^2V-U+(\tau\gamma)^{-1}V,\qquad \mathbf{x}\in\Omega\,,$$

$$\text{(1.2b)}\qquad \tau V_t=D\Delta V-V+1-\tau\gamma\left(\alpha\left(\mathbf{x}\right)U^2V-U\right)-\beta\gamma U,\qquad \mathbf{x}\in\Omega\,,$$

with homogeneous Neumann boundary conditions, and where $\Omega=[0,1]\times[0,d_y]$. Here Δ is the 2-D Laplacian, and the domain aspect ratio $d_y\equiv L_y/L_x$ is assumed to satisfy $0<d_y<1$, which represents a thin cell. The other dimensionless parameters in (1.2) are defined in terms of the original parameters by

$$\text{(1.3a)}\qquad \varepsilon^2\equiv\frac{D_1}{L_x^2(c+r)}\,,\qquad D\equiv\frac{D_2}{L_x^2k_1}\,,\qquad \tau\equiv\frac{c+r}{k_1}\,,\qquad \beta\equiv\frac{r}{k_1}\,,$$

and the primary bifurcation parameter γ in this system is given, as in [4, 6], by

$$\text{(1.3b)}\qquad \gamma\equiv\frac{(c+r)k_1^2}{k_{20}b^2}\,.$$

In the original dimensional model of [6], $D_1\ll D_2$ are the diffusivities for U and V, respectively, b is the rate of production of inactive ROP (source parameter), c is the

bioRxiv preprint doi: https://doi.org/10.1101/114876; this version posted March 7, 2017. The copyright holder for this preprint (which was not certified by peer review) is the author/funder. All rights reserved. No reuse allowed without permission.

rate constant for deactivation, r is the rate constant describing active ROPs being used up in cell softening and subsequent hair formation (loss parameter), and the activation step is assumed to be proportional to $k_1 V + k_{20}\alpha(\mathbf{x})U^2 V$. The activation and overall auxin level within the cell, initiating an autocatalytic reaction, is represented by $k_1 > 0$ and $k_{20} > 0$ respectively. The parameter k_{20}, appearing in the bifurcation parameter γ of (1.3b), plays a key role for pattern formation in the model (see [6, 28] for more details on model formulation).

We will examine the role that geometrical features, such as the 2-D domain and the auxin-gradient, play on the dynamics of localized regions, referred to as spots, where the active-ROP has an elevated concentration. This analysis is an extension to the analysis performed in [4], where it was shown that a 1-D localized stripe pattern of active-ROP in a 2-D domain will, generically, exhibit breakup into spatially localized spots. To analyze the subsequent dynamics and stability of these localized spots in the presence of the auxin gradient, we will extend the hybrid asymptotic-numerical methodology developed in [8, 21, 22, 30] for prototypical RD systems with spatially homogeneous coefficients. This analysis will lead to a novel finite-dimensional dynamical system characterizing slow spot evolution. Although in our numerical simulations we will focus on the two specific forms for the auxin gradient in (1.1), our analysis applies to an arbitrary gradient.

The outline of the paper is as follows. In section 2 we introduce the basic scaling for (1.2), and we use singular perturbation methods to construct an N-spot quasi steady-state solution. In section 3 we derive a differential algebraic system (DAE) of ODEs coupled to a nonlinear algebraic system, which describes the slow dynamics of the centers of a collection of localized spots. In particular, we explore the role that the auxin gradient (i) in (1.1) has on the ultimate spatial alignment of the localized spots that result from the breakup of an interior stripe. For the auxin gradient (i) of (1.1), in section 4 we briefly examine the onset of spot self-replication instabilities and other $\mathcal{O}(1)$ time-scale instabilities of quasi steady-state solutions. In section 5 we examine the effect on spot dynamics induced by the more biologically realistic model auxin (ii) of (1.1). To illustrate the theory, throughout the paper we perform various numerical simulations and numerical bifurcation analyses using the parameter sets in Table 1 (cf. [6]). A brief discussion in section 6 concludes the paper.

2. Asymptotic Regime for Spot Formation. We shall assume a shallow, thin cell, which will be modelled as a 2D flat rectangular domain, as shown in Figure 1. In this domain, the biochemical interactions leading to an RH initiation process are assumed to be governed by the RD model (1.2).

For an RD system, a spatial pattern in 2-D consisting of spots is understood as a collection of structures where, at least, one of its solution components is highly localized. These structures typically evolve in such a manner that the spatial locations of the spots change slowly in time. However, depending on the parameter regime, these localized patterns can also exhibit fast $\mathcal{O}(1)$ time-scale instabilities, leading either to spot creation or destruction. For prototypical RD systems such as the Gierer–Meinhardt, Gray–Scott, Schnakenberg, and Brusselator models, the slow dynamics of localized solutions and the possibility of self-replication and competition instabilities, leading either to spot creation or destruction, respectively, have been studied using a hybrid asymptotic-numerical approach in [8, 21, 22, 30]. In addition, in the large diffusion limit, and to leading-order in $-1/\log\varepsilon$, the linear stability analysis for localized spot patterns characterizing competition instabilities can be reduced to the study of classes of nonlocal eigenvalue problems (NLEPs). Rigorous

bioRxiv preprint doi: https://doi.org/10.1101/114876; this version posted March 7, 2017. The copyright holder for this preprint (which was not certified by peer review) is the author/funder. All rights reserved. No reuse allowed without permission.

Parameter sets:

One		Two	
Original	***Re-scaled***	***Original***	***Re-scaled***
$D_1 = 0.075$	$\varepsilon^2 = 1.02 \times 10^{-4}$	$D_1 = 0.1$	$\varepsilon^2 = 3.6 \times 10^{-4}$
$D_2 = 20$	$D = 0.51$	$D_2 = 10$	$D = 0.4$
$k_1 = 0.008$	$\tau = 18.75$	$k_1 = 0.01$	$\tau = 11$
$b = 0.008$	$\beta = 6.25$	$b = 0.01$	$\beta = 1$
$c = 0.1$		$c = 0.1$	
$r = 0.05$		$r = 0.01$	
$k_{20} \in [10^{-3}, 2.934]$	$\gamma \in [150, 0.051]$	$k_{20} \in [0.01, 1.0]$	$\gamma \in [11, 0.11]$
$L_x = 70$		$L_x = 50$	
$L_y = 29.848$	$d_y = 0.4211$	$L_y = 20$	$d_y = 0.40$

TABLE 1

Two parameter sets in the original and dimensionless re-scaled variables. The fundamental units of length and time are μm and sec, and concentration rates are measured by an arbitrary datum (con) per time unit; k_{20} is measured by con^2/s, and diffusion coefficients units are $\mu m/s^2$.

results for the spectral properties of various NLEPs corresponding to 2-D steady-state spot patterns, 1-D spike patterns, and 1-D homoclinic stripe patterns, are given in [20, 21, 30, 31, 32, 33, 34, 35] (see also the references therein).

Our companion studies in [6] of 1-D spike patterns and in [4] of 1-D stripe patterns has extended these previous NLEP analyses of prototypical RD systems to the more complicated, and biologically realistic, plant root-hair system (1.2). In the analysis below we will extend the 2-D hybrid asymptotic-numerical methodology developed in [8, 21, 22, 30] for prototypical RD systems to (1.2). The primary new feature in (1.2), not considered in these previous works, is to analyze in detail the effect of a spatial gradient in the differential operator in (1.2), which represents variations in the auxin distribution. This spatial gradient is shown to play a key role in the spatial alignment of the localized structures.

To initiate our hybrid approach for (1.2), we first need to rescale the RD model (1.2) in Ω in order to determine the parameter regime where localized spots exist. To do so, we can readily show as in Proposition 2.2 of [6] for the 1-D problem, that for any steady-state solution $U_0(\mathbf{x})$ of (1.2) we must have

$$\int_\Omega U_0(\mathbf{x})\, d\mathbf{x} = \frac{|\Omega|}{\beta\gamma}\,, \tag{2.4}$$

where $|\Omega| = d_y$ is the area of Ω. Since the parameters d_y, β and γ are $\mathcal{O}(1)$, the constraint (2.4) implies that the average of U across the whole domain is also $\mathcal{O}(1)$. In other words, if we seek localized solutions such that $U \to 0$ away from localized $\mathcal{O}(\varepsilon)$ regions near a collection of spots, then from (2.4) we must have that $U = \mathcal{O}\left(\varepsilon^{-2}\right)$ near each spot.

2.1. A Multiple-Spot Quasi Steady-State Pattern. As a first step to derive a finite-dimensional dynamical system for the slow dynamics of active-ROP spots, we must construct a quasi steady-state pattern that describes ROP aggregation in N small spatially segregated regions.

To do so, we now seek a quasi steady-state solution where U is localized within an $\mathcal{O}(\varepsilon)$ region near each spot $\mathbf{x}_j$ for $j = 1, \ldots, N$. From the conservation law (2.4) this

bioRxiv preprint doi: https://doi.org/10.1101/114876; this version posted March 7, 2017. The copyright holder for this preprint (which was not certified by peer review) is the author/funder. All rights reserved. No reuse allowed without permission.

implies that $U = \mathcal{O}\left(\varepsilon^{-2}\right)$ near each spot. In this way, if we replace $U = \varepsilon^{-2} U_j$ near each spot, and define $\boldsymbol{\xi} = \varepsilon^{-1}\left(\mathbf{x} - \mathbf{x}_j\right)$, we obtain from (2.4) that $\sum_{j=1}^{N} \int_{\mathbb{R}^2} U_j \, d\boldsymbol{\xi} \sim d_y/(\beta\gamma)$. This simple scaling law motivates the introduction of the new variables u, v and D_0 defined by

$$U = \varepsilon^{-2} u\,, \quad V = \varepsilon^{2} v\,, \quad D = \varepsilon^{-2} D_0\,. \tag{2.5}$$

In terms of these new variables, (1.2) becomes

$$u_t = \varepsilon^2 \Delta u + \alpha(\mathbf{x}) u^2 v - u + \varepsilon^4 (\tau\gamma)^{-1} v\,, \qquad \mathbf{x} \in \Omega\,, \tag{2.6a}$$

$$\tau \varepsilon^2 v_t = D_0 \Delta v - \varepsilon^2 v + 1 - \varepsilon^{-2}\left[\tau\gamma\left(\alpha\left(\mathbf{x}\right) u^2 v - u\right) + \beta\gamma u\right]\,, \qquad \mathbf{x} \in \Omega\,. \tag{2.6b}$$

$$\partial_n u = 0\,, \quad \partial_n v = 0\,, \qquad \mathbf{x} \in \partial\Omega\,. \tag{2.6c}$$

Next, in the inner region near the j-th spot we construct the inner expansion for the spot profile, where the leading-order terms are locally radially symmetric. We expand this inner solution as

$$u = u_{0j}\left(\rho\right) + \varepsilon u_{1j} + \cdots\,, \qquad v = v_{0j}\left(\rho\right) + \varepsilon v_{1j} + \cdots\,, \quad \rho = |\boldsymbol{\xi}| \equiv \varepsilon^{-1}|\mathbf{x} - \mathbf{x}_j|\,. \tag{2.7}$$

Substituting (2.7) into the steady-state problem for (2.6), we obtain the leading-order radially symmetric problem

$$\begin{aligned} &\Delta_\rho u_{0j} + \alpha\left(\mathbf{x}_j\right) u_{0j}^2 v_{0j} - u_{0j} = 0\,, \\ &D_0 \Delta_\rho v_{0j} - \tau\gamma\left(\alpha\left(\mathbf{x}_j\right) u_{0j}^2 v_{0j} - u_{0j}\right) - \beta\gamma u_{0j} = 0\,, \end{aligned} \qquad 0 < \rho < \infty\,, \tag{2.8}$$

where $\Delta_\rho \equiv \partial_{\rho\rho} + \rho^{-1}\partial_\rho$ is the Laplacian operator in polar co-ordinates. As a remark, in our derivation of the spot dynamics in section 3 we will need to retain the next term in the Taylor series of the auxin distribution, representing the auxin gradient in the regions where active-ROP is localized, which is given by

$$\alpha\left(\mathbf{x}\right) = \alpha\left(\mathbf{x}_j\right) + \varepsilon \nabla\alpha\left(\mathbf{x}_j\right) \cdot \boldsymbol{\xi} + \cdots\,, \qquad \text{where } \boldsymbol{\xi} \equiv \varepsilon^{-1}\left(\mathbf{x} - \mathbf{x}_j\right). \tag{2.9}$$

As we show below in section 3, this higher-order approximation is key to deriving the dynamical system for spot dynamics.

We consider (2.8) together with the boundary conditions

$$u_{0j}'(0) = v_{0j}'(0) = 0\,; \quad u_{0j} \to 0\,, \quad v_{0j} \sim S_j \log\rho + \chi\left(S_j\right) + o(1)\,, \quad \text{as } \rho \to \infty\,, \tag{2.10}$$

where S_j is called the *source parameter*. The correction term $\chi_j = \chi(S_j)$ in the far-field behavior is determined from

$$\lim_{\rho\to\infty}\left(v_{0j} - S_j \log\rho\right) = \chi(S_j)\,. \tag{2.11}$$

By integrating the equation for v_{0j} in (2.8), and using the limiting behavior $v_{0j} \sim S_j \log\rho$ as $\rho \to \infty$, we readily obtain the identity

$$S_j = \frac{\beta\gamma}{D_0} \int_0^\infty \left[\frac{\tau}{\beta}\left(\alpha\left(\mathbf{x}_j\right) u_{0j}^2 v_{0j} - u_{0j}\right) + u_{0j}\right] \rho \, d\rho\,. \tag{2.12}$$

Then, upon using the change of variables

$$u_{0j} \equiv \sqrt{\frac{D_0}{\beta\gamma\alpha\left(\mathbf{x}_j\right)}}\, u_c\,, \qquad v_{0j} \equiv \sqrt{\frac{\beta\gamma}{D_0\alpha\left(\mathbf{x}_j\right)}}\, v_c\,, \tag{2.13}$$

bioRxiv preprint doi: https://doi.org/10.1101/114876; this version posted March 7, 2017. The copyright holder for this preprint (which was not certified by peer review) is the author/funder. All rights reserved. No reuse allowed without permission.

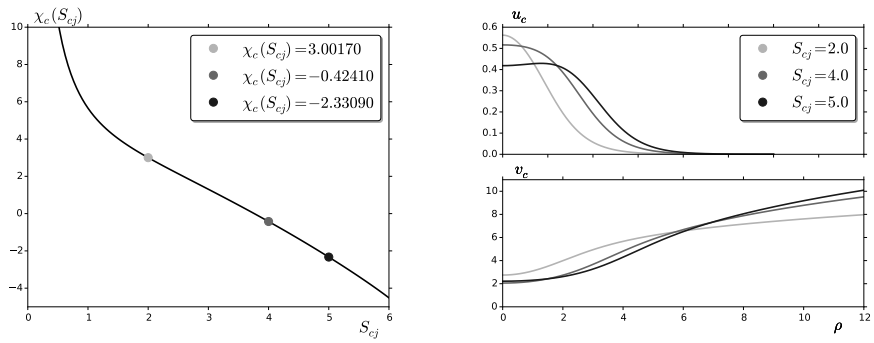

(a) (b)

FIG. 2. *(a) The constant $\chi_c(S_{cj})$ versus the source parameter S_{cj}, as computed numerically from (2.14). In (b) we plot the radially symmetric solution u_c (upper panel) and v_c (bottom panel), respectively, of (2.14) at the values of S_{cj} as shown in the legend. We use Parameter set One from Table 1, for which $\tau/\beta = 3$.*

the system (2.8) reduces to what we refer to as the *canonical core problem* (CCP), which consists of

$$\Delta_\rho u_c + u_c^2 v_c - u_c = 0\,, \qquad \Delta_\rho v_c - \frac{\tau}{\beta}\left(u_c^2 v_c - u_c\right) - u_c = 0\,, \tag{2.14a}$$

on $0 < \rho < \infty$, together with the following boundary conditions where S_{cj} is a parameter:

$$u_c'(0) = v_c'(0) = 0, \quad u_c \to 0\,, \quad v_c \sim S_{cj}\log\rho + \chi_c\left(S_{cj}\right) + o(1)\,, \quad \text{as } \rho \to \infty\,. \tag{2.14b}$$

Comparing (2.13) with (2.10), we observe that S_j and $\chi(S_j)$ are related to S_{cj} and $\chi_c(S_{cj})$ by

$$S_j \equiv \sqrt{\frac{\beta\gamma}{D_0\alpha\left(\mathbf{x}_j\right)}}\, S_{cj}\,, \qquad \chi(S_j) \equiv \sqrt{\frac{\beta\gamma}{D_0\alpha\left(\mathbf{x}_j\right)}}\, \chi_c\left(S_{cj}\right)\,. \tag{2.15}$$

To numerically compute solutions to (2.14) we use the MATLAB code BVP4C and solve the resulting BVP on the large, but finite, interval $[0, \rho_0]$, for a range of values of S_{cj}. The constant $\chi_c\left(S_{cj}\right)$ is identified from $v_c\left(\rho_0\right) - S_c \log\rho_0 = \chi_c$, where v_c is the numerically computed solution. In our simulations $\rho_0 = 12$ was sufficient to provide a few digits of accuracy. The results of our computation are shown in Figure 2(a) where we plot $\chi_c\left(S_{cj}\right)$ versus S_{cj}. In Figure 2(b) we also plot u_c and v_c at a few values of S_{cj}. We observe that $u_c(\rho)$ has a volcano-shaped profile when $S_{cj} = 5$.

We remark that the CCP (2.14) depends only on the ratio τ/β, which characterizes the deactivation and removal rates of active-ROP (see (1.3a)). This implies that the CCP (2.14) only describes the aggregation process. On the other hand, notice that (2.13) and (2.15) reveal the role that the auxin plays on the activation process. The scaling (2.13) is such that the further from the left boundary active-ROP localizes, the larger the solution amplitude. This feature will be confirmed by numerical simulations in subsection 2.2. In addition, the scaling of the source-parameter in (2.15) indicates that the auxin controls the inactive-ROP distribution along the cell. That

bioRxiv preprint doi: https://doi.org/10.1101/114876; this version posted March 7, 2017. The copyright holder for this preprint (which was not certified by peer review) is the author/funder. All rights reserved. No reuse allowed without permission.

is, while S_{cj} characterizes how v interacts with u in the region where a spot occurs, the parameter S_j will be determined by the inhomogeneous distribution of source points, which are also governed by the auxin gradient. In other words, the gradient controls and catalyzes the switching process, which leads to localized elevations of concentration of active-ROP.

Next, we examine the outer region away from the spots centered at $\mathbf{x}_1, \ldots, \mathbf{x}_N$. To leading-order, we obtain from the steady-state problem in (2.6a) that $u_0 \sim \varepsilon^4 v_0/(\beta\gamma)$. Upon substituting this expression into the reaction terms of (2.6b), we obtain in the outer region that

$$-\varepsilon^2 v_0 + 1 - \varepsilon^{-2}\left[\tau\gamma\left(\alpha\left(\mathbf{x}\right)u_0^2 v_0 - u_0\right) + \beta\gamma u_0\right] = 1 + \mathcal{O}\left(\varepsilon^2\right) . \tag{2.16}$$

Then, we calculate the effect of the localized spots on the outer equation for v. Assuming $u \sim u_j$ and $v \sim v_j$ near the j-th spot, we readily calculate in the sense of distributions that as $\varepsilon \to 0$

$$\begin{aligned} &\varepsilon^{-2}\left[\tau\gamma\left(\alpha\left(\mathbf{x}\right)u_j^2 v_j - u_j\right) + \beta\gamma u_j\right] \\ &\qquad \to 2\pi\left(\int_0^\infty \left[\tau\gamma\left(\alpha\left(\mathbf{x}_j\right)u_{0j}^2 v_{0j} - u_{0j}\right) + \beta\gamma u_{0j}\right]\rho\, d\rho\right)\delta(\mathbf{x}-\mathbf{x}_j) \\ &\qquad = 2\pi D_0 S_j \delta(\mathbf{x}-\mathbf{x}_j) . \end{aligned} \tag{2.17}$$

Combining (2.16), (2.17) and (2.6b) we obtain that the leading-order outer solution v_0, in the region away from $\mathcal{O}(\varepsilon)$ neighborhoods of the spots, satisfies

$$\Delta v_0 + \frac{1}{D_0} = 2\pi\sum_{i=1}^{N} S_i \delta\left(\mathbf{x}-\mathbf{x}_i\right) , \quad \mathbf{x}\in\Omega ; \qquad \partial_n v_0 = 0 , \quad \mathbf{x}\in\partial\Omega . \tag{2.18a}$$

By using (2.10) to match the outer and inner solutions for v, we must solve (2.18a) subject to the following singularity behavior as $\mathbf{x}\to\mathbf{x}_j$:

$$v_0 \sim S_j \log|\mathbf{x}-\mathbf{x}_j| + \frac{S_j}{\sigma} + \chi(S_j) , \quad \text{for } j = 1,\ldots,N, \text{ where } \sigma \equiv -\frac{1}{\log\varepsilon}. \tag{2.18b}$$

We now proceed to solve (2.18) for v_0 and derive a nonlinear algebraic system for the source parameters $S_{c1}, \ldots, S_{cN}$. To do so, we introduce the unique Neumann Green's function $G(\mathbf{x};\mathbf{y})$ satisfying (cf. [21])

$$\Delta G = \frac{1}{d_y} - \delta\left(\mathbf{x}-\mathbf{y}\right) , \quad \int_\Omega G\left(\mathbf{x};\mathbf{y}\right)\, d\mathbf{y} = 0 , \quad \mathbf{x}\in\Omega , \qquad \partial_n G = 0 , \quad \mathbf{x}\in\partial\Omega .$$

This Green's function satisfies the reciprocity relation $G\left(\mathbf{x};\mathbf{y}\right) = G\left(\mathbf{y};\mathbf{x}\right)$, and can be globally decomposed as

$$G\left(\mathbf{x};\mathbf{y}\right) = -\frac{1}{2\pi}\log|\mathbf{x}-\mathbf{y}| + R\left(\mathbf{x};\mathbf{y}\right) ,$$

where $R\left(\mathbf{x};\mathbf{y}\right)$ is the smooth regular part of $G\left(\mathbf{x};\mathbf{y}\right)$. For $\mathbf{x}\to\mathbf{y}$, this Green's function has the local behavior

$$G\left(\mathbf{x};\mathbf{y}\right) \sim -\frac{1}{2\pi}\log|\mathbf{x}-\mathbf{y}| + R\left(\mathbf{y};\mathbf{y}\right) + \nabla_{\mathbf{x}} R\left(\mathbf{y};\mathbf{y}\right)\cdot\left(\mathbf{x}-\mathbf{y}\right) + \mathcal{O}\left(|\mathbf{x}-\mathbf{y}|^2\right) .$$

Moreover, an explicit infinite series solution for G and its regular part R in the rectangle Ω is available (cf. [21]).

bioRxiv preprint doi: https://doi.org/10.1101/114876; this version posted March 7, 2017. The copyright holder for this preprint (which was not certified by peer review) is the author/funder. All rights reserved. No reuse allowed without permission.

In terms of this Green's function, the solution to (2.18a) is

$$v_0 = -2\pi \sum_{i=1}^{N} S_i G\left(\mathbf{x};\mathbf{x}_i\right) + \bar{v}_0\,, \qquad \text{where} \qquad \sum_{i=1}^{N} S_i = \frac{d_y}{2\pi D_0}\,. \tag{2.19}$$

Here $\bar{v}_0$ is a constant to be found. The condition on S_i in (2.19) arises from the Divergence Theorem applied to (2.18). We then expand v_0 as $\mathbf{x} \to \mathbf{x}_j$ and enforce the required singularity behavior (2.18b). This yields that

$$\frac{S_j}{\sigma} + \chi\left(S_j\right) = -2\pi S_j R_j - 2\pi \sum_{i=1}^{N} S_i G_{ji} + \bar{v}_0\,, \qquad \text{for} \quad j = 1, \ldots N\,. \tag{2.20}$$

Here $G_{ji} \equiv G\left(\mathbf{x}_j;\mathbf{x}_i\right)$ and $R_j \equiv R\left(\mathbf{x}_j;\mathbf{x}_j\right)$. The system (2.20), together with the constraint in (2.19), defines a nonlinear algebraic system for the $N+1$ unknowns $\bar{v}_0$ and $S_1, \ldots, S_N$.

It is convenient to rewrite this system in matrix form. To do so, we define $\mathbf{e} \equiv (1, \ldots, 1)^T$, $\mathbf{S} \equiv (S_1, \ldots, S_N)^T$, $\boldsymbol{\chi} \equiv (\chi(S_1), \ldots, \chi(S_N))^T$ and

$$\mathbf{G} \equiv \begin{pmatrix} R_1 & G_{12} & \cdots & G_{1N} \\ G_{21} & \ddots & & \vdots \\ \vdots & & \ddots & G_{N-1N} \\ G_{N1} & \cdots & G_{NN-1} & R_N \end{pmatrix}, \quad \mathbf{E} \equiv \frac{\mathbf{e}\mathbf{e}^T}{N} = \frac{1}{N}\begin{pmatrix} 1 & \cdots & 1 \\ \vdots & \ddots & \vdots \\ 1 & \cdots & 1 \end{pmatrix},$$

where $G_{ij} = G_{ji}$. Then, the system (2.20), together with the constraint in (2.19), can be written as

$$\mathbf{S} + 2\pi\sigma\mathbf{G}\mathbf{S} = \sigma\left(\bar{v}_0\mathbf{e} - \boldsymbol{\chi}\right)\,, \qquad \mathbf{e}^T\mathbf{S} = \frac{d_y}{2\pi D_0}\,. \tag{2.21}$$

Left multiplying the first equation in (2.21) by $\mathbf{e}^T$, and using the second equation in (2.21), we find an expression for $\bar{v}_0$

$$\bar{v}_0 = \frac{1}{N\sigma}\left(\frac{d_y}{2\pi D_0} + 2\pi\sigma\mathbf{e}^T\mathbf{G}\mathbf{S} + \sigma\mathbf{e}^T\boldsymbol{\chi}\right)\,. \tag{2.22}$$

Substituting $\bar{v}_0$ back into the first equation of (2.21), we obtain a nonlinear system for $S_1, \ldots, S_N$ given by

$$\mathbf{S} + \sigma\left(\mathbf{I} - \mathbf{E}\right)\left(2\pi\mathbf{G}\mathbf{S} + \boldsymbol{\chi}\right) = \frac{d_y}{2\pi N D_0}\mathbf{e}\,. \tag{2.23}$$

In terms of $\mathbf{S}$, $\bar{v}_0$ is given in (2.22). In addition, to relate S_j and χ_j with the CCP (2.14), we define

$$\boldsymbol{\alpha} \equiv \operatorname{diag}\left(\frac{1}{\sqrt{\alpha\left(\mathbf{x}_1\right)}}, \ldots, \frac{1}{\sqrt{\alpha\left(\mathbf{x}_N\right)}}\right), \quad \mathbf{S}_c \equiv \begin{pmatrix} S_{c1} \\ \vdots \\ S_{cN} \end{pmatrix}, \quad \boldsymbol{\chi}_c \equiv \begin{pmatrix} \chi_c\left(S_{c1}\right) \\ \vdots \\ \chi_c\left(S_{cN}\right) \end{pmatrix}.$$

Then, by using (2.15), we find

$$\mathbf{S} = \omega\boldsymbol{\alpha}\mathbf{S}_c\,, \qquad \boldsymbol{\chi} = \omega\boldsymbol{\alpha}\boldsymbol{\chi}_c\,, \qquad \omega \equiv \sqrt{\frac{\beta\gamma}{D_0}}\,. \tag{2.24}$$

Finally, upon substituting (2.24) into (2.23) we obtain our main result regarding quasi steady-state spot patterns.

bioRxiv preprint doi: https://doi.org/10.1101/114876; this version posted March 7, 2017. The copyright holder for this preprint (which was not certified by peer review) is the author/funder. All rights reserved. No reuse allowed without permission.

PROPOSITION 1. *Let $0 < \varepsilon \ll 1$ and assume $D_0 = \mathcal{O}(1)$ in (2.6) so that $D = \mathcal{O}\left(\varepsilon^{-2}\right)$ in (1.2). Suppose that the nonlinear algebraic system for the source parameters, given by*

$$\boldsymbol{\alpha}\mathbf{S}_c + \sigma\left(\mathbf{I} - \mathbf{E}\right)\left(2\pi\mathbf{G}\boldsymbol{\alpha}\mathbf{S}_c + \boldsymbol{\alpha}\boldsymbol{\chi}_c\right) = \frac{d_y}{2\pi\omega N D_0}\mathbf{e}\,, \tag{2.25a}$$

$$\bar{v}_0 = \frac{1}{N\sigma}\left(\frac{d_y}{2\pi D_0} + 2\pi\omega\mathbf{e}^T\mathbf{G}\boldsymbol{\alpha}\mathbf{S}_c + \sigma\omega\mathbf{e}^T\boldsymbol{\chi}_c\right)\,, \tag{2.25b}$$

has a solution for the given spatial configuration $\mathbf{x}_1, \ldots, \mathbf{x}_N$ of spots. Then, there is a quasi steady-state solution for (1.2) with $U = \varepsilon^{-2}u$ and $V = \varepsilon^2 v$. In the outer region away from the spots, we have $u = \mathcal{O}(\varepsilon^4)$ and $v \sim v_0$, where v_0 is given asymptotically in terms of $\mathbf{S} = \omega\boldsymbol{\alpha}\mathbf{S}_c$ by (2.19). In contrast, in the j-th inner region near $\mathbf{x}_j$, we have

$$u \sim \sqrt{\frac{D_0}{\beta\gamma\alpha\left(\mathbf{x}_j\right)}}\,u_c\,, \qquad v \sim \sqrt{\frac{\beta\gamma}{D_0\alpha\left(\mathbf{x}_j\right)}}\,v_c\,, \tag{2.26}$$

where u_c and v_c is the solution of the CCP (2.14) in terms of S_{cj} satisfying (2.25a).

2.2. Spots and Baby Droplets. Proposition 1 provides an asymptotic characterization of a N-spot quasi steady-state solution. As has been previously studied in the companion paper [4], localized spots can be generated by the breakup of a straight homoclinic stripe. The numerical simulations in Figure 3 illustrate how small spots are formed from the breakup of an interior homoclinic stripe and how they evolve slowly in time to a steady-state two-spot pattern aligned with the direction of the auxin gradient. As shown in Figure 3(c)–Figure 3(d), the amplitude of the left-most spot grows smaller as the spot drifts towards the left domain boundary at $X = 0$, while the amplitude of the right-most spot grows at it drifts towards the right domain boundary at $X = L_x$. The spot profiles are described by Proposition 1 for each fixed re-scaled variables $\mathbf{x}_j$. Our simulations below of slow spot dynamics will confirm the numerical results in Figure 3(d) that the spots become aligned with the direction of the auxin gradient.

In order to explore solutions that bifurcate from a multi-spot steady state, we adapted the MATLAB code of [1, 29] and performed a numerical continuation for the RD system (1.2) in the bifurcation parameter k_{20}, starting from the solution in Figure 3(d) (all other as in Parameter set One in Table 1). The results are shown in Figure 4. In the bifurcation diagram depicted in Figure 4(a) the linearly stable branch is plotted as a solid curve and unstable ones by light gray-dashed curves. We found fold bifurcations and a pitchfork bifurcation, represented by filled circles and an empty hexagon, where the stability properties of solutions changed and symmetry breaking properties occur, respectively. Further fold bifurcations, where the stability property remains unchanged, are also detected. Overall our results suggest that a homoclinic snaking-like structure occurs in our 2-D context, qualitatively similar in form to that found in [4] for the corresponding 1-D system. This intricate structure consists of a cascade where each step is determined by fold points—not explicitly shown in Figure 4(a)—, with an extra spot emerging on each step. A pattern consisting of a spot and a peanut-form is found in solution branch labelled as P. This solution is shown in Figure 4(c).

We found that peanut-form and baby droplet solution are unstable steady-states in this region of parameter space, hence they do not persist in time. In addition, as

bioRxiv preprint doi: https://doi.org/10.1101/114876; this version posted March 7, 2017. The copyright holder for this preprint (which was not certified by peer review) is the author/funder. All rights reserved. No reuse allowed without permission.

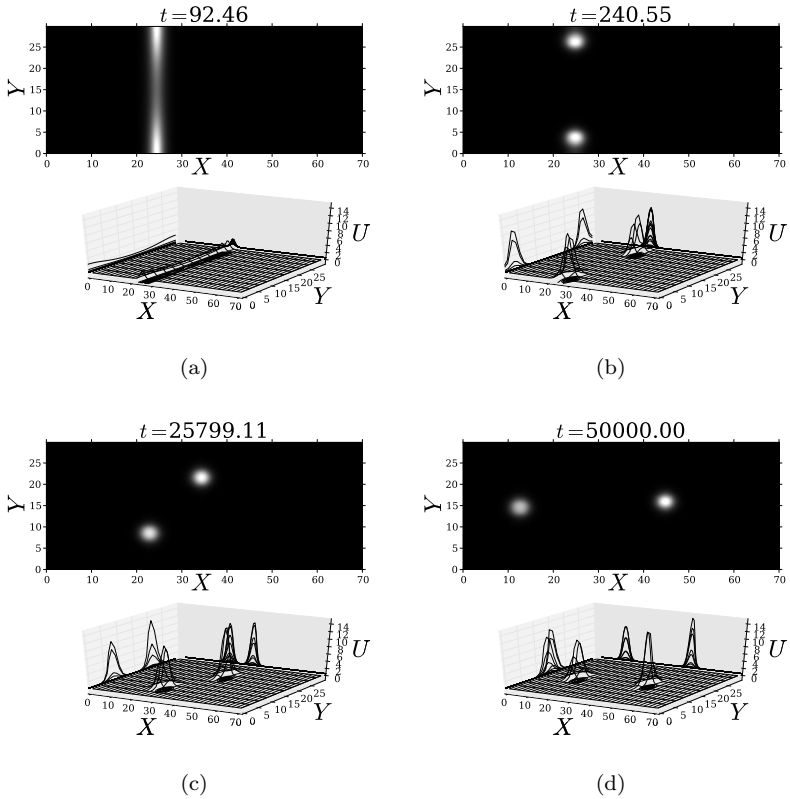

FIG. 3. *Breakup instability of an interior localized homoclinic stripe for U, and the resulting slow spot dynamics. (a) The localized stripe initially breaks into two spots; (b) once formed, the spots migrate from the boundary towards each other in the vertical direction, and then (c) rotate until they get aligned with the longitudinal direction. (d) Finally, they get pinned far from each other along the y-midline by the auxin gradient. Parameter Set One from Table 1 was used with $k_{20} = 0.5$. For these values the initial steady-state stripe is centered at $X_0 = 24.5$. Figure from [4].*

can be seen in Figure 4(b), there are stable multi-spot solutions when k_{20} is small enough. This implies that certain $\mathcal{O}(1)$ time-scale instabilities play an important role in transitioning between steady-state patterns.

3. The Slow Dynamics of Spots. In subsection 2.1 we constructed an N-spot quasi steady-state solution for an arbitrary, but "frozen", spatial configuration $\mathbf{x}_1, \ldots, \mathbf{x}_N$ of localized patches of active-ROP. In this section, we derive a differential-algebraic system of ODEs (DAE) for the slow time-evolution of $\mathbf{x}_1, \ldots, \mathbf{x}_N$ towards their equilibrium locations in Ω. This system will consist of a constraint that involves the slow time evolution of the source parameters $S_{c1}, \ldots, S_{cN}$. The derivation of this DAE system is an extension of the 1-D analysis of [6].

To derive the DAE system, we must extend the analysis in subsection 2.1 by retaining the $\mathcal{O}(\varepsilon)$ terms in (2.7) and (2.9). By allowing the spot locations to depend on the slow time scale $\eta = \varepsilon^2 t$ as $\mathbf{x}_j = \mathbf{x}_j(\eta)$, we obtain in the j-th inner region that

bioRxiv preprint doi: https://doi.org/10.1101/114876; this version posted March 7, 2017. The copyright holder for this preprint (which was not certified by peer review) is the author/funder. All rights reserved. No reuse allowed without permission.

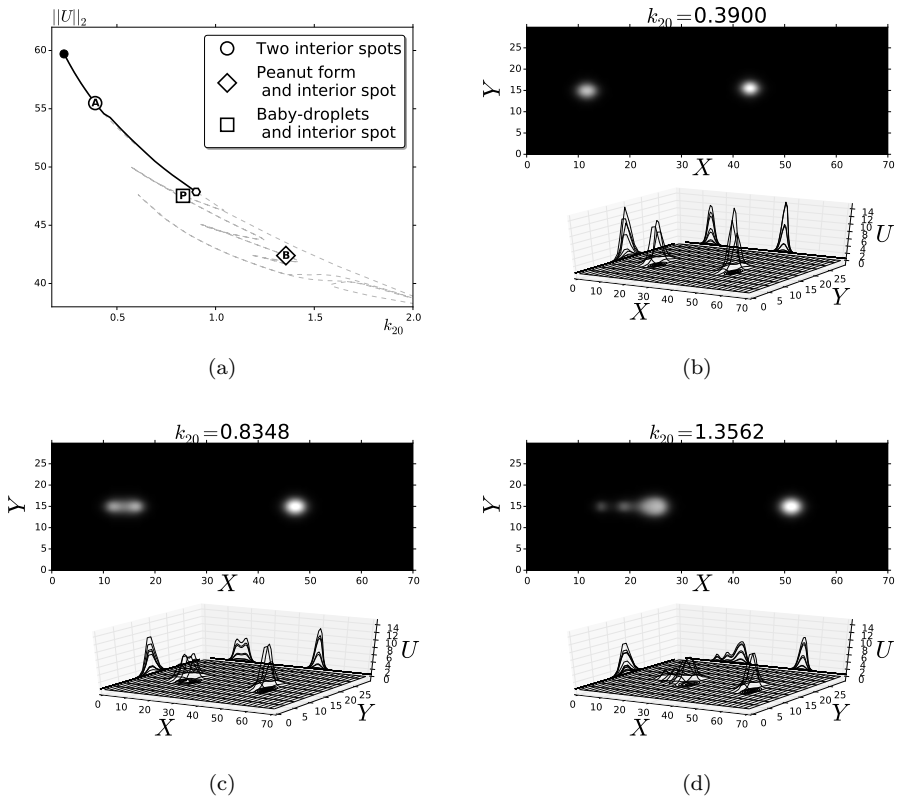

FIG. 4. *(a) Bifurcation diagram as k_{20} is varied showing a stable branch, labelled A, of (b) two spots, and unstable branches (light gray-dashed curves). Filled circle at $k_{20}^o = 0.2319$ is a fold bifurcation and the empty hexagon at $k_{20}^* = 0.90161$ is a pitchfork bifurcation. (c) A peanut-form and one spot steady-state, from label P in (a). (d) A two-spot with baby droplets steady-state solution, from label B in (a). Parameter Set One was used, as given in Table 1. See k_{20} values for each steady-state on top of upper panels in (b)-(d).*

the corrections terms u_{1j} and v_{1j} to the CCP (2.14) satisfy

$$\Delta u_{1j} + \alpha(\mathbf{x}_j)\left(v_{1j}u_{0j}^2 + 2u_{0j}u_{1j}v_{0j}\right) - u_{1j} = -\frac{d\mathbf{x}_j}{d\eta}\cdot\nabla u_{0j} - \boldsymbol{\xi}\cdot\nabla\alpha(\mathbf{x}_j)\,u_{0j}^2 v_{0j}\,,$$
$$D_0\Delta v_{1j} - \tau\gamma\left[\alpha(\mathbf{x}_j)\left(v_{1j}u_{0j}^2 + 2u_{0j}u_{1j}v_{0j}\right) - u_{1j}\right] - \beta\gamma u_{1j} = \tau\gamma\boldsymbol{\xi}\cdot\nabla\alpha(\mathbf{x}_j)\,u_{0j}^2 v_{0j}\,.$$

Introducing the vector $\mathbf{Q}_1$ and the matrix $\mathbf{M}$ by

$$\mathbf{Q}_1 \equiv \begin{pmatrix} u_{1j} \\ v_{1j} \end{pmatrix}, \qquad \mathbf{M} \equiv \begin{pmatrix} 2\alpha_j u_{0j}v_{0j} - 1 & \alpha_j u_{0j}^2 \\ -\dfrac{\tau\gamma}{D_0}\left(2\alpha_j u_{0j}v_{0j} - 1\right) - \dfrac{\beta\gamma}{D_0} & -\dfrac{\tau\gamma}{D_0}\alpha_j u_{0j}^2 \end{pmatrix}, \tag{3.27}$$

where we have defined $\alpha_j \equiv \alpha(\mathbf{x}_j)$, we obtain

$$\Delta\mathbf{Q}_1 + \mathbf{M}\mathbf{Q}_1 = \begin{pmatrix} -\dfrac{d\mathbf{x}_j}{d\eta}\cdot\nabla u_{0j} \\ 0 \end{pmatrix} + \left(\boldsymbol{\xi}\cdot\nabla\alpha_j\right)u_{0j}^2 v_{0j}\begin{pmatrix} -1 \\ \dfrac{\tau\gamma}{D_0} \end{pmatrix}, \tag{3.28a}$$

bioRxiv preprint doi: https://doi.org/10.1101/114876; this version posted March 7, 2017. The copyright holder for this preprint (which was not certified by peer review) is the author/funder. All rights reserved. No reuse allowed without permission.

where we have labelled $\nabla\alpha_j \equiv \nabla\alpha(\mathbf{x}_j)$. To determine the far-field behavior for $\mathbf{Q}_1$, we expand the outer solution v_0 in (2.19) as $\mathbf{x} \to \mathbf{x}_j$ and retain the $\mathcal{O}(\varepsilon)$ terms. In this way, we obtain

$$\mathbf{Q}_1 \to \begin{pmatrix} 0 \\ \boldsymbol{\zeta}_j \cdot \boldsymbol{\xi} \end{pmatrix}, \quad \text{as} \quad \rho \equiv |\boldsymbol{\xi}| \to \infty\,, \tag{3.28b}$$

where we posed

$$\boldsymbol{\zeta}_j \equiv -2\pi \left(S_j \nabla_{\mathbf{x}} R_j + \sum_{i \neq j}^{N} S_i \nabla_{\mathbf{x}} G_{ji} \right), \qquad j = 1, \ldots, N\,, \tag{3.28c}$$

the numbers S_j are determined from (2.23), and

$$\nabla_{\mathbf{x}} R_j \equiv \nabla_{\mathbf{x}} R\left(\mathbf{x}_j; \mathbf{x}_j\right), \qquad \nabla_{\mathbf{x}} G_j \equiv \nabla_{\mathbf{x}} G\left(\mathbf{x}_j; \mathbf{x}_j\right), \qquad j = 1, \ldots, N\,. \tag{3.28d}$$

In order to impose a solvability condition on (3.28), which ultimately leads to an ODE for the spot locations, we first must rewrite (3.28) in terms of the canonical variables (2.13) associated with the CCP (2.14). Using this transformation, the right-hand side of (3.28a) becomes

$$\begin{aligned} &\begin{pmatrix} -\dfrac{d\mathbf{x}_j}{d\eta} \cdot \nabla u_{0j} \\ 0 \end{pmatrix} + \left(\boldsymbol{\xi} \cdot \nabla\alpha_j\right) u_{0j}^2 v_{0j} \begin{pmatrix} -1 \\ \dfrac{\tau\gamma}{D_0} \end{pmatrix} = \\ &\qquad \sqrt{\frac{D_0}{\beta\gamma\alpha_j}} \left[\begin{pmatrix} -\dfrac{d\mathbf{x}_j}{d\eta} \cdot \nabla u_c \\ 0 \end{pmatrix} + \boldsymbol{\xi} \cdot \frac{\nabla\alpha_j}{\alpha_j} u_c^2 v_c \begin{pmatrix} -1 \\ \dfrac{\tau\gamma}{D_0} \end{pmatrix} \right]. \end{aligned} \tag{3.29}$$

In addition, the matrix $\mathbf{M}$ on the left-hand side of (3.28a) becomes

$$\mathbf{M} = \begin{pmatrix} 2u_c v_c - 1 & \dfrac{D_0}{\beta\gamma} u_c^2 \\ -\dfrac{1}{D_0}\left(\tau\gamma\left(2u_c v_c - 1\right) + \beta\gamma\right) & -\dfrac{\tau}{\beta} u_c^2 \end{pmatrix}. \tag{3.30}$$

Together with (3.29) this suggests that we introduce new variables $\hat{u}_1$ and $\hat{v}_1$ defined by

$$u_{1j} \equiv \sqrt{\frac{D_0}{\beta\gamma\alpha_j}}\, \hat{u}_1\,, \qquad v_{1j} \equiv \frac{\beta\gamma}{D_0} \sqrt{\frac{D_0}{\beta\gamma\alpha_j}}\, \hat{v}_1\,.$$

In terms of these new variables, and upon substituting (3.29) and (3.30) into (3.28),

bioRxiv preprint doi: https://doi.org/10.1101/114876; this version posted March 7, 2017. The copyright holder for this preprint (which was not certified by peer review) is the author/funder. All rights reserved. No reuse allowed without permission.

we obtain that $\hat{\mathbf{Q}}_1 \equiv (\hat{u}_1, \hat{v}_1)^T$ satisfies

(3.31a)
$$\mathcal{L}\hat{\mathbf{Q}}_1 \equiv \Delta\hat{\mathbf{Q}}_1 + \mathbf{M}_c\hat{\mathbf{Q}}_1 = \begin{pmatrix} -\dfrac{d\mathbf{x}_j}{d\eta}\cdot\nabla u_c \\ 0 \end{pmatrix} + \boldsymbol{\xi}\cdot\frac{\nabla\alpha_j}{\alpha_j}u_c^2 v_c \begin{pmatrix} -1 \\ \dfrac{\tau}{\beta} \end{pmatrix}, \qquad \boldsymbol{\xi}\in\mathbb{R}^2,$$

(3.31b)
$$\hat{\mathbf{Q}}_1 \to \begin{pmatrix} 0 \\ \hat{\boldsymbol{\zeta}}_j\cdot\boldsymbol{\xi} \end{pmatrix} \quad \text{as} \quad \rho\equiv|\boldsymbol{\xi}|\to\infty,$$

(3.31c)
$$\text{where} \quad \hat{\boldsymbol{\zeta}}_j \equiv -2\pi\left(S_{cj}\nabla_{\mathbf{x}}R_j + \sum_{i\neq j}^{N} S_{ci}\nabla_{\mathbf{x}}G_{ji}\right),$$

and S_{cj} for $j=1,\ldots,N$ satisfies the nonlinear algebraic system (2.25a). In addition, in (3.31a) $\mathbf{M}_c$ is defined by

(3.31d)
$$\mathbf{M}_c \equiv \begin{pmatrix} 2u_cv_c - 1 & u_c^2 \\ -\dfrac{\tau}{\beta}(2u_cv_c-1)-1 & -\dfrac{\tau}{\beta}u_c^2 \end{pmatrix},$$

where u_c and v_c satisfy the CCP (2.14), which is parametrized by S_{cj}.

In (3.31c), the source parameters S_{cj} depend indirectly on the auxin distribution through the nonlinear algebraic system (2.25), as summarized in Proposition 1. We further observe from the second term on the right-hand side of (3.31a) that its coefficient $\nabla\alpha_j/\alpha_j$ is independent of the magnitude of the spatially inhomogeneous distribution of auxin, but instead depends on the direction of the gradient.

3.1. Solvability Condition. We now derive a DAE system for the spot dynamics by applying a solvability condition to (3.31). We let $\boldsymbol{\xi} = (\xi_1,\xi_2)^T$ and define $\mathbf{u}_c \equiv (u_c, v_c)^T$. Differentiating the core problem (2.14a) with respect to the i-th coordinate ξ_i of $\boldsymbol{\xi}$, we obtain

$$\mathcal{L}\left(\partial_{\xi_i}\mathbf{u}_c\right) = \mathbf{0}, \qquad \text{where} \qquad \partial_{\xi_i}\mathbf{u}_c \equiv \begin{pmatrix} u_c'(\rho) \\ v_c'(\rho) \end{pmatrix}\frac{\xi_i}{\rho}, \quad \text{for} \quad i=1,2.$$

This shows that the dimension of the nullspace of $\mathcal{L}$ in (3.31), and hence its adjoint $\mathcal{L}^\star$, is at least two-dimensional. We will assume that this nullspace is exactly two-dimensional, as can be readily verified numerically provided that S_j does not coincide with the spot self-replication threshold given in subsection 4.1 below.

We first seek two independent nontrivial solutions to the homogeneous adjoint problem $\mathcal{L}^\star\boldsymbol{\Psi} \equiv \Delta\boldsymbol{\Psi} + \mathbf{M}_c^T\boldsymbol{\Psi} = \mathbf{0}$ in the form $\boldsymbol{\Psi}_i \equiv \mathbf{P}(\rho)\xi_i/\rho$ for $i=1,2$. We readily derive that $\mathbf{P}$ satisfies

(3.32)
$$\Delta_\rho\mathbf{P} - \frac{1}{\rho^2}\mathbf{P} + \mathbf{M}_c^T\mathbf{P} = \mathbf{0}, \qquad 0<\rho<\infty; \qquad \mathbf{P}\sim\begin{pmatrix} 0 \\ \dfrac{1}{\rho} \end{pmatrix} \quad \text{as} \quad \rho\to\infty,$$

where the condition at infinity in (3.32) is used as a normalization condition for $\mathbf{P}$.

Next, to derive our solvability condition we use Green's identity over a large disk

bioRxiv preprint doi: https://doi.org/10.1101/114876; this version posted March 7, 2017. The copyright holder for this preprint (which was not certified by peer review) is the author/funder. All rights reserved. No reuse allowed without permission.

Ω_{ρ_0} of radius $|\boldsymbol{\xi}| = \rho_0 \gg 1$ to obtain

$$\lim_{\rho_0\to\infty}\int_{\Omega_{\rho_0}}\left(\boldsymbol{\Psi}_i^T\mathcal{L}\hat{\mathbf{Q}}_1 - \hat{\mathbf{Q}}_1\mathcal{L}^\star\boldsymbol{\Psi}_i\right)d\boldsymbol{\xi} = \lim_{\rho_0\to\infty}\int_{\partial\Omega_{\rho_0}}\left(\boldsymbol{\Psi}_i^T\partial_\rho\hat{\mathbf{Q}}_1 - \hat{\mathbf{Q}}_1\partial_\rho\boldsymbol{\Psi}_i\right)\Big|_{\rho=\rho_0} dS\,, \tag{3.33}$$

for $i = 1, 2$. With $\boldsymbol{\Psi}_i \equiv \mathbf{P}(\rho)y_i/\rho$, and for a fixed $i \in \{1, 2\}$, we first calculate the left-hand side (LHS) of this expression using (3.31a) to obtain with $\mathbf{P} \equiv (P_1(\rho), P_2(\rho))^T$ that

$$\begin{aligned}
\text{LHS} &= \lim_{\rho_0\to\infty}\int_{\Omega_{\rho_0}}\left(-\boldsymbol{\Psi}_i^T\begin{pmatrix}\mathbf{x}_j'\cdot\nabla u_c\\ 0\end{pmatrix} + \boldsymbol{\Psi}_i^T\left(\boldsymbol{\xi}\cdot\frac{\nabla\alpha_j}{\alpha_j}\right)\begin{pmatrix}-1\\ \tau/\beta\end{pmatrix}u_c^2v_c\right)d\boldsymbol{\xi}\\
&= \lim_{\rho_0\to\infty}\left[-\int_{\Omega_{\rho_0}}P_1\frac{\xi_i}{\rho}\sum_{k=1}^{2}x_{jk}'u_c'(\rho)\frac{\xi_k}{\rho}\,d\boldsymbol{\xi} + \frac{\nabla\alpha_j}{\alpha_j}\cdot\int_{\Omega_{\rho_0}}\boldsymbol{\xi}\left(-P_1+\frac{\tau}{\beta}P_2\right)\frac{\xi_i}{\rho}u_c^2v_c\,d\boldsymbol{\xi}\right],\\
&= \lim_{\rho_0\to\infty}\left[-x_{ji}'\int_{\Omega_{\rho_0}}P_1\frac{\xi_i^2}{\rho^2}u_c'(\rho)\,d\boldsymbol{\xi} + \frac{(\nabla\alpha_j)_i}{\alpha_j}\int_{\Omega_{\rho_0}}\frac{\xi_i^2}{\rho}\left(-P_1+\frac{\tau}{\beta}P_2\right)u_c^2v_c\,d\boldsymbol{\xi}\right],\\
&= -x_{ji}'\pi\int_0^\infty P_1u_c'(\rho)\rho\,d\rho + \frac{\pi(\nabla\alpha_j)_i}{\alpha_j}\int_0^\infty\left(-P_1+\frac{\tau}{\beta}P_2\right)u_c^2v_c\rho^2\,d\rho\,.
\end{aligned}$$

Here $\mathbf{x}_j' \equiv (x_{j1}', x_{j2}')^T$. In deriving the result above, we used the identity

$$\int_{\Omega_{\rho_0}}\xi_i\xi_k f(\rho)\,d\boldsymbol{\xi} = \delta_{ik}\pi\int_0^{\rho_0}\rho^3 f(\rho)\,d\rho$$

for any radially symmetric function $f(\rho)$, where δ_{ik} is the Kronecker delta.

Next, we calculate the right-hand side (RHS) of (3.33) using the far-field behaviors of $\hat{\mathbf{Q}}_1$ and $\mathbf{P}$ as $\rho\to\infty$. We derive that

$$\begin{aligned}
\text{RHS} &= \lim_{\rho_0\to\infty}\int_{\partial\Omega_{\rho_0}}\left(P_2\frac{y_i}{\rho}\partial_\rho\left(\hat{\boldsymbol{\zeta}}_j\cdot\boldsymbol{\xi}\right) - \hat{\boldsymbol{\zeta}}_j\cdot\boldsymbol{\xi}\,\partial_\rho\left(P_2\frac{\xi_i}{\rho}\right)\right)dS\,,\\
&= \lim_{\rho_0\to\infty}\int_{\partial\Omega_{\rho_0}}\left(P_2\frac{\xi_i^2}{\rho^2}\hat{\boldsymbol{\zeta}}_{ji} - \left(\hat{\boldsymbol{\zeta}}_j\cdot\boldsymbol{\xi}\right)\frac{\xi_i}{\rho}\partial_\rho P_2\right)dS\,,\\
&= \lim_{\rho_0\to\infty}\int_{\partial\Omega_{\rho_0}}\frac{2\xi_i^2}{\rho^3}\hat{\boldsymbol{\zeta}}_{ji}\,dS = 2\pi\hat{\boldsymbol{\zeta}}_{ji}\,.
\end{aligned}$$

In the last passage, we used $dS = \rho_0 d\theta$ where θ is the polar angle. Finally, we equate LHS and RHS for $i = 1, 2$, and write the resulting expression in vector form:

$$-\mathbf{x}_j'\pi\int_0^\infty P_1u_c'\rho\,d\rho + \pi\frac{\nabla\alpha_j}{\alpha_j}\int_0^\infty\left(\frac{\tau}{\beta}P_2 - P_1\right)u_c^2v_c\rho^2\,d\rho = 2\pi\hat{\boldsymbol{\zeta}}_j\,. \tag{3.34}$$

We summarize our main result for spot dynamics as follows:

PROPOSITION 2. *Under the same assumptions as Proposition 1, and assuming that the N-spot quasi steady-state solution is stable on an $\mathcal{O}(1)$ time-scale, the slow dynamics on the long time-scale $\eta = \varepsilon^2 t$ of this quasi steady-state spot pattern consists of the constraints (2.25) coupled to the ODEs*

$$\frac{d\mathbf{x}_j}{d\eta} = n_1\hat{\boldsymbol{\zeta}}_j + n_2\frac{\nabla\alpha_j}{\alpha_j}, \qquad \hat{\boldsymbol{\zeta}}_j \equiv -2\pi\left(S_{cj}\nabla_{\mathbf{x}}R_j + \sum_{i\neq j}^{N}S_{ci}\nabla_{\mathbf{x}}G_{ji}\right)\,. \tag{3.35a}$$

bioRxiv preprint doi: https://doi.org/10.1101/114876; this version posted March 7, 2017. The copyright holder for this preprint (which was not certified by peer review) is the author/funder. All rights reserved. No reuse allowed without permission.

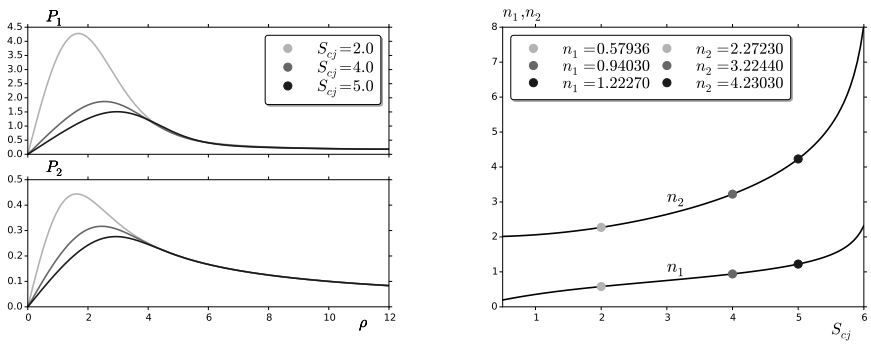

(a) (b)

FIG. 5. *(a) Numerical solution of the adjoint solution satisfying (3.32) for* $\mathbf{P} = (P_1, P_2)^T$ *for values of* S_{cj} *as shown in the legend;* P_1 *(top panel) and* P_2 *(bottom panel). (b) Numerical results for the solvability condition integrals* n_1 *and* n_2*, defined in (3.35b), as* S_{cj} *increases. The filled circles correspond to* S_{cj} *values in (a). We use Parameter set One from Table 1, for which* $\tau/\beta = 3$*.*

for $j = 1, \ldots, N$*. The constants* n_1 *and* n_2*, which depend on* S_{cj} *and the ratio* τ/β *are defined in terms of the solution to the CCP (2.14) and the homogeneous adjoint solution (3.32) by*

$$n_1 \equiv -\frac{2}{\displaystyle\int_0^\infty P_1 u_c' \rho \, d\rho}, \qquad n_2 \equiv \frac{\displaystyle\int_0^\infty \left(\frac{\tau}{\beta} P_2 - P_1\right) u_c^2 v_c \rho^2 \, d\rho}{\displaystyle\int_0^\infty P_1 u_c' \rho \, d\rho}. \tag{3.35b}$$

In (3.35a), the source parameters S_{cj} *satisfy the nonlinear algebraic system (2.25), which depends on the instantaneous spatial configuration of the* N *spots. Overall, this leads to a DAE system characterizing slow spot dynamics.*

Proposition 2 describes the slow dynamics of a collection of N localized spots under an arbitrary, but smooth, spatially dependent auxin gradient. It is an extension of the 1-D analysis of spike evolution, considered in [6]. The dynamics in (3.35a), shows that the spot locations depend on the gradient of the Green's function, which depends on the domain Ω, as well as the spatial gradient of the auxin distribution. In particular, the spot dynamics depends only indirectly on the magnitude of the auxin distribution $\alpha(\mathbf{x}_j)$ through the source parameter S_{cj}. The auxin gradient $\nabla\alpha_j$, however, is essential to determining the true steady-state spatial configuration of spots. In addition, the spatial interaction between the spots arises from the terms in the finite sum of (3.35a), mediated by the Green's function. Since the Green's function and its regular part can be evaluated for a rectangular domain (cf. [21]), we can readily use (3.35) to numerically track the slow time-evolution of a collection of spots for a specified auxin gradient.

Before illustrating results from the DAE dynamics, we must first determine the constants n_1 and n_2 as a function of S_{cj} for a prescribed value of the ratio τ/β. This ratio is associated with the linear terms in the kinetics of the original dimensional system (1.2), which are related to the spontaneous deactivation of ROPs and production of other biochemical complexes which promote cell wall softening (cf. [6, 28]). To determine n_1 and n_2, we first solve the adjoint problem (3.32) numerically using

bioRxiv preprint doi: https://doi.org/10.1101/114876; this version posted March 7, 2017. The copyright holder for this preprint (which was not certified by peer review) is the author/funder. All rights reserved. No reuse allowed without permission.

the MATLAB routine BVP4C. This is done by enforcing the required local behavior that $\mathbf{P} = \mathcal{O}(\rho)$ as $\rho \to 0$ and by imposing the far-field behavior for $\mathbf{P}$, given in (3.32), at $\rho = \rho_0 = 12$. In Figure 5(a) we plot P_1 and P_2 for three values of S_{cj}, where $\tau/\beta = 3$, and Parameter set One in Table 1 was used. For each of the three values of S_{cj}, we observe from this figure that the far-field behavior $P_2(\rho) \sim 1/\rho$ and $P_1(\rho) \sim (\tau/\beta - 1)/\rho$ as $\rho \to \infty$, which is readily derived from (3.32), is indeed satisfied. Moreover, after performing the required quadratures in (3.35b), in Figure 5(b) we plot n_1 and n_2 versus S_{cj}. These numerical results show that $n_1 > 0$ and $n_2 > 0$ for $S_{cj} > 0$.

3.2. Comparison Between Theory and Asymptotics for Slow Spot Dynamics. In this subsection we compare predictions from our asymptotic theory for slow spot dynamics with corresponding full numerical results computed from (2.6) using a spatial mesh with 500 and 140 gridpoints in the x and y directions, respectively. For the time-stepping a modified Rosenbrock formula of order 2 was used.

The procedure to obtain numerical results from our asymptotic DAE system in Proposition 2 is as follows. This DAE system is solved numerically by using Newton's method to solve the nonlinear algebraic system (2.25) together with a Runge-Kutta ODE solver to evolve the dynamics in (3.35a). The solvability integrals $n_1(S)$ and $n_2(S)$ in the dynamics (3.35a) and the function $\chi(S)$ in the nonlinear algebraic system (2.25) are pre-computed at 200 grid points in S and a cubic spline interpolation is fitted to the discretely sampled functions to compute them at arbitrary values of S. For the rectangular domain, explicit expressions for the Green's functions G and R, together with their gradients, as required in the DAE system, are calculated from the expressions in §4 of [21].

To compare our results for slow spot dynamics we use Parameter set One of Table 1 and take $k_{20} = 0.3$. For the auxin gradient we took the monotone 1-D gradient in type (i) in (1.1). By a small perturbation of the unstable 1-D stripe solution, our full numerical computations of (2.6) lead to the creation of two localized spots. Numerical values for the centers of the two spots are calculated (see the caption of Figure 6) and these values are used as the initial conditions for our numerical solution of the DAE system in Proposition 2. In Figure 6 we compare our full numerical results for the x and y coordinates for the spot trajectories, as computed from the RD system (2.6), and those computed from the corresponding DAE system. The key distinguishing feature in these results is that the spots become aligned to the longitudinal midline of the domain. We observe that the y-components of the spot trajectories are predicted rather accurately over long time intervals by the DAE system. The x-components of the trajectories are initially close, but then deviate slightly as t increases.

4. Fast $\mathcal{O}(1)$ Time-Scale Instabilities. We now briefly examine the stability properties of the N-spot quasi-equilibrium solution of Proposition 1 to $\mathcal{O}(1)$ time-scale instabilities, which are fast relative to the slow dynamics. We first consider spot self-replication instabilities associated with non-radially symmetric perturbations near each spot.

4.1. The Self-Replication Threshold. Since the speed of the slow spot drift is $\mathcal{O}(\varepsilon^2) \ll 1$, in our stability analysis below we will assume that the spots are "frozen" at some configuration $\mathbf{x}_1, \ldots, \mathbf{x}_N$. We will consider the possibility of instabilities that are locally non-radially symmetric near each spot. In the inner region near the j-th spot at $\mathbf{x}_j$, where $\boldsymbol{\xi} = \varepsilon^{-1}(\mathbf{x} - \mathbf{x}_j)$, we linearize (2.6) around the leading-order core

bioRxiv preprint doi: https://doi.org/10.1101/114876; this version posted March 7, 2017. The copyright holder for this preprint (which was not certified by peer review) is the author/funder. All rights reserved. No reuse allowed without permission.

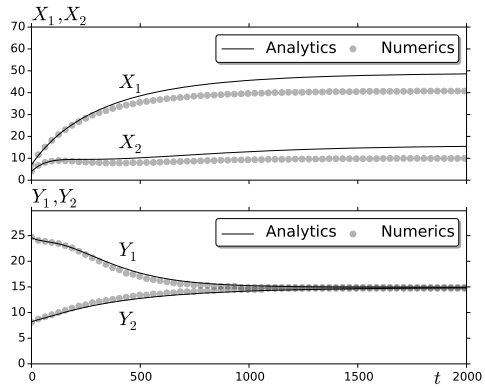

FIG. 6. *The time-dependent location of two spots for an auxin gradient of the type (i) in (1.1) as obtained from the DAE system (solid curves) in Proposition 2 with* $k_{20} = 0.3$ *and with the other parameters as in Parameter set One of Table 1. The initial locations for the two spots are* $x_1(0) = 7.0$, $y_1(0) = 8.21$ *and* $x_2(0) = 3.97$, $y_2(0) = 24.63$. *The full numerical results computed from (1.2) are the filled circles. Observe that the DAE system predicts that the two spots become aligned along the longitudinal midline of the cell. The* x*-coordinate (top panel) and the* y*-coordinate (bottom panel) of the two spots.*

solution u_{0j}, v_{0j}, satisfying (2.8), by writing

$$u = u_{0j} + e^{\lambda t}\phi_{0j}\,, \qquad v = v_{0j} + e^{\lambda t}\psi_{0j}\,. \tag{4.36}$$

From (2.6), we obtain to leading order that

$$\begin{aligned}
&\Delta_{\boldsymbol{\xi}}\phi_{0j} + \alpha(\mathbf{x}_j)\left(u_{0j}^2\psi_{0j} + 2u_{0j}v_{0j}\phi_{0j}\right) - \phi_{0j} = \lambda\phi_{0j},\\
&D_0\Delta_{\boldsymbol{\xi}}\psi_{0j} - \tau\gamma\left[\alpha(\mathbf{x}_j)\left(u_{0j}^2\psi_{0j} + 2u_{0j}v_{0j}\phi_{0j}\right) - \phi_{0j}\right] - \beta\gamma\phi_{0j} = 0,
\end{aligned}$$

where $\Delta_{\boldsymbol{\xi}}$ denotes the Laplacian in the local variable $\boldsymbol{\xi}$. Then, using the re-scaling

$$u_{0j} \equiv \sqrt{\frac{D_0}{\beta\gamma\alpha\left(\mathbf{x}_j\right)}}\,u_c\,, \qquad v_{0j} \equiv \sqrt{\frac{\beta\gamma}{D_0\alpha\left(\mathbf{x}_j\right)}}\,v_c\,, \qquad \psi_{0j} = \frac{\beta\gamma}{D_0}\tilde{\psi}_{0j}\,,$$

as motivated by (2.13), the system above reduces to

$$\begin{aligned}
&\Delta_{\boldsymbol{\xi}}\phi_{0j} + \tilde{\psi}_{0j}u_c^2 + 2u_cv_c\phi_{0j} - \phi_{0j} = \lambda\phi_{0j}\,,\\
&\Delta_{\boldsymbol{\xi}}\tilde{\psi}_{0j} + \left(\frac{\tau}{\beta} - 1 - \frac{2\tau}{\beta}u_cv_c\right)\phi_{0j} - \frac{\tau}{\beta}u_c^2\tilde{\psi}_{0j} = 0\,,
\end{aligned} \tag{4.37}$$

where u_c, v_c is the solution to the CCP (2.14).

We then look for an $\mathcal{O}(1)$ time-scale instability associated with the local angular integer mode $m \geq 1$ by introducing the new variables $\Phi_0(\rho)$ and $\Psi_0(\rho)$ defined by

$$\phi_{0j} = e^{im\theta}\Phi_0(\rho)\,, \quad \tilde{\psi}_{0j} = e^{im\theta}\Psi_0(\rho)\,, \quad \text{where } \rho = |\boldsymbol{\xi}|,\ \boldsymbol{\xi} = \varepsilon^{-1}(\mathbf{x} - \mathbf{x}_j)\,, \tag{4.38}$$

and $\boldsymbol{\xi}^T = \rho(\cos\theta, \sin\theta)$. Substituting (4.38) into (4.37), we obtain the following eigenvalue problem:

$$\begin{aligned}
&\mathcal{L}_m\Phi_0 + (2u_cv_c - 1)\,\Phi_0 + u_c^2\Psi_0 = \lambda\Phi_0\,,\\
&\mathcal{L}_m\Psi_0 + \left(\frac{\tau}{\beta} - 1 - \frac{2\tau}{\beta}u_cv_c\right)\Phi_0 - \frac{\tau}{\beta}u_c^2\Psi_0 = 0\,,
\end{aligned} \qquad 0 \leq \rho < \infty\,. \tag{4.39}$$

bioRxiv preprint doi: https://doi.org/10.1101/114876; this version posted March 7, 2017. The copyright holder for this preprint (which was not certified by peer review) is the author/funder. All rights reserved. No reuse allowed without permission.

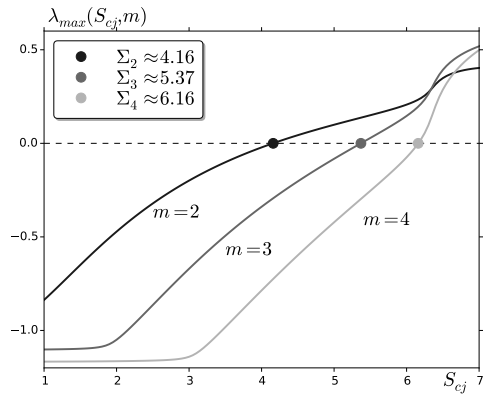

FIG. 7. *The largest real-valued eigenvalue λ_{max} of (4.39) versus S_{cj} for different angular modes m. The peanut-splitting thresholds Σ_m for different m are indicated by filled circles. Parameter set One of Table 1, where $\tau/\beta = 3$, was used.*

Here we have defined $\mathcal{L}_m \Upsilon \equiv \partial_{\rho\rho}\Upsilon + \rho^{-1}\partial_\rho \Upsilon - m^2\rho^{-2}\Upsilon$. We impose the usual regularity condition for Φ_0 and Ψ_0 at $\rho = 0$. The appropriate far-field boundary conditions for (4.39) is discussed below.

The eigenvalue problem (4.39) is not amenable to analysis. Therefore, we solve it numerically for various integer values of m. We denote $\lambda_{\max}$ to be the eigenvalue of (4.39) with the largest real part. Since u_c and v_c depend on S_{cj} from the CCP (2.14), we have implicitly that $\lambda_{\max} = \lambda_{\max}(S_{cj}, m)$. To determine the onset of any instabilities, for each m we compute the smallest threshold value $S_{cj} = \Sigma_m$ where $\mathrm{Re}(\lambda_{\max}(\Sigma_m, m)) = 0$. In our computations, we only consider $m = 2, 3, 4, \ldots$, since $\lambda_{\max} = 0$ for any value of S_{cj} for the translational mode $m = 1$. Any such instability for $m = 1$ is reflected in instability in the DAE system (3.35a).

For $m \geq 2$ we impose the far-field behavior that Φ_0 decays exponentially as $\rho \to \infty$ while $\Psi_0 \sim \mathcal{O}(\rho^{-m}) \to 0$ as $\rho \to \infty$. With this limiting behavior, (4.39) is discretized with centered differences on a large but finite domain. We then determine $\lambda_{\max}(S_{cj}, m)$ by computing the eigenvalues of the discretized eigenvalue problem, in matrix form. For $m \geq 2$ our computations show that $\lambda_{\max}(S_{cj}, m)$ is real and that $\lambda_{\max}(S_{cj}, m) > 0$ only when $S_{cj} > \Sigma_m$. In our computations we took 400 meshpoints on the interval $0 \leq \rho < 15$. For the ratio $\tau/\beta = 3$, corresponding to Parameter set One of Table 1, the results for the threshold values Σ_m for $m = 2, 3, 4$ given in Figure 7 are insensitive to increasing either the domain length or the number of grid points. Our main conclusion is that as S_{cj} is increased, the solution profile of the j-th spot first becomes unstable to a non-radially symmetric peanut-splitting mode, corresponding to $m = 2$, as S_{cj} increases above the threshold $\Sigma_2 \approx 4.16$ when $\tau/\beta = 3$. As a remark, if we take $\tau/\beta = 11$, corresponding to Parameter set Two of Table 1, we compute instead that $\Sigma_2 \approx 3.96$.

To illustrate this peanut-splitting threshold, we consider a pattern with a single localized spot. Using (2.19) we find $S_1 = d_y/(2\pi D_0)$. Then, (2.15) yields the following expression for the source parameter for the CCP (2.14)

$$S_{c1} = \frac{d_y}{2\pi}\sqrt{\frac{\alpha(x_1)}{D_0\beta\gamma}}\,. \tag{4.40}$$

bioRxiv preprint doi: https://doi.org/10.1101/114876; this version posted March 7, 2017. The copyright holder for this preprint (which was not certified by peer review) is the author/funder. All rights reserved. No reuse allowed without permission.

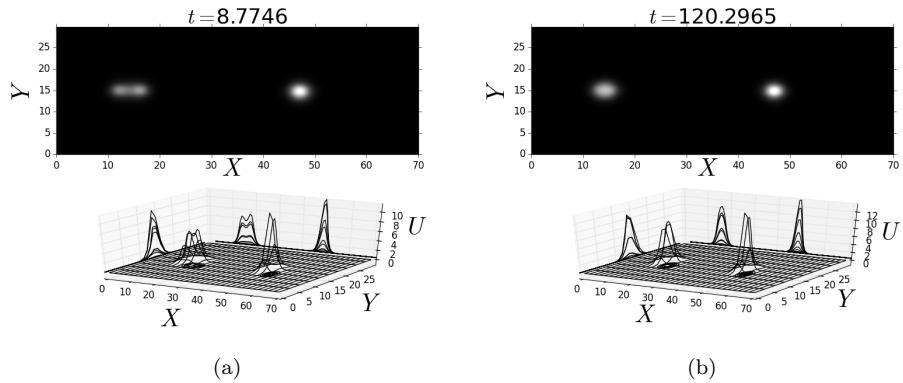

(a) (b)

FIG. 8. *Two snapshots of a time-dependent numerical simulation where a peanut-form merges into a spot. (a) Peanut-form and a spot. (b) Two spots. Parameter set One as given in Table 1 and* $k_{20} = 0.8108$.

When $\tau/\beta = 3$, corresponding to Parameter set One of Table 1, we predict that the one-spot pattern will first undergo a shape-deformation, due to the $m = 2$ peanut-splitting mode, when S_{c1} exceeds the threshold $\Sigma_2 \approx 4.16$. Since γ is inversely proportional to the parameter k_{20}, as shown in (1.3b), which determines the auxin level, we predict that as the auxin level is increased above a threshold a peanut-form will develop from a solitary spot. As shown below in subsection 4.2 for an auxin distribution of the type (i) in (1.1), this linear peanut-splitting instability triggers a nonlinear spot replication event.

4.2. Numerical Illustrations of $\mathcal{O}(1)$ Time-Scale Instabilities. In Figure 4(c) we showed a steady-state solution consisting of a spot and a peanut-form, which is obtained as a result of numerical continuation in the bifurcation parameter k_{20}. This solution belongs to the unstable branch labelled by P in Figure 4(a), which is confined between two fold bifurcations (not explicitly shown). We take a solution from this branch as an initial condition in Figure 8(a) for a time-dependent numerical simulation of the full RD model (1.2) using a centered finite-difference scheme. Our numerical results in Figure 8(b) show that this initial state evolves dynamically into a stable two-spot solution. This is a result of the overlapping of the stable branch A with an unstable one in the bifurcation diagram of Figure 4(a). In addition, in Figure 9 we plot the source parameters corresponding to the two-spot steady-state aligned along the midline $Y = Ly/2$ as the parameter k_{20} is varied. These asymptotic results, which asymptotically characterize states in branch A of Figure 4(a), are computed from the steady-state of the DAE system (3.35). Notice that the spot closest to the left-hand boundary loses stability at $k_{20} \approx 0.851$, when S_{c1} meets the peanut-splitting threshold Σ_2. On the other hand, S_{c2} values corresponding to the spot closest to the right-hand boundary are always below Σ_2. Hence, no shape change for this spot is observed. This result rather accurately predicts the pitchfork bifurcation in Figure 4(a) portrayed by an empty pentagon at $k_{20} \approx 0.902$.

Other initial conditions and parameter ranges exhibit $\mathcal{O}(1)$ time-scale instabilities. To illustrate these instabilities, and see whether a self-replication spot process is triggered by a linear peanut-splitting instability, we perform a direct numerical simulation of the full RD model (1.2) taking as initial condition the unstable steady-state

bioRxiv preprint doi: https://doi.org/10.1101/114876; this version posted March 7, 2017. The copyright holder for this preprint (which was not certified by peer review) is the author/funder. All rights reserved. No reuse allowed without permission.

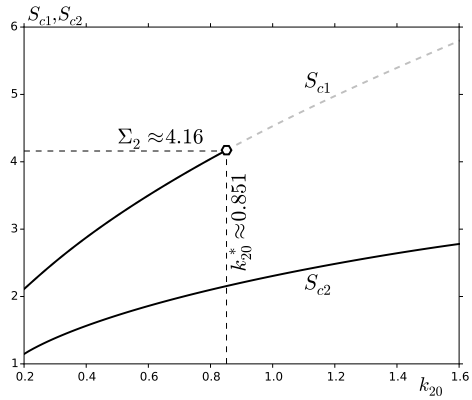

FIG. 9. *Source parameters for a two-spot steady-state solution of the DAE system*(3.35) *as* k_{20} *is varied. Stable profiles are denoted by the solid curves, and the spot closest to the left boundary at* $x = 0$ *is unstable to shape deformation on the dashed curve, which begins at* $k_{20} \approx 0.851$. *This value is the asymptotic prediction of the pitchfork bifurcation point in Figure* 4(a) *drawn by an empty pentagon. Parameter set One of Table* 1 *was used.*

solution labelled by B in Figure 4(a). This steady-state, shown in Figure 10(a), consists of two spots, with one having four small droplets associated with it. The time evolution of this initial condition is then shown in the different panels of Figure 10. Firstly, we observe in Figure 10(b) that the small droplets for the left-most spot in Figure 10(a) are annihilated in $\mathcal{O}(1)$ times. Then, the right-most spot, which has a relatively low source parameter owing to its distance away from the left-hand boundary, is annihilated on an $\mathcal{O}(1)$ time-scale triggered by a linear competition instability. The solitary remaining spot at $(X_1, Y_1) = (28, 14.9240)$, shown in Figure 10(c), now has a source parameter $S_{c1} = 9.1403$, given in (4.40) of subsection 4.1, that exceeds the peanut-splitting threshold $\Sigma_2 \approx 4.16$. This linear shape-deforming instability gives rise to the peanut-form shown in Figure 10(d), and the direction of spot-splitting is aligned with the direction of the monotone decreasing auxin gradient, which depends only on the longitudinal direction. In Figure 10(e) and Figure 10(f) we show that this linear peanut-splitting instability has triggered a nonlinear spot-splitting event that creates a second localized spot. Finally, these two spots drift away from each other and their resulting slow dynamics is characterized by the DAE dynamics in Proposition 2.

Competition and self-replication instabilities, such as illustrated above, are two types of fast $\mathcal{O}(1)$ time-scale instabilities that commonly occur for localized spot patterns in singularly perturbed RD systems. Although it is beyond the scope of this paper to give a detailed analysis of a competition instability for our plant RD model (1.2), based on analogies with other RD models (cf. [8, 21, 22, 30]), this instability typically occurs when the source parameter of a particular spot is below some threshold or, equivalently, when there are too many spots that can be supported in the domain for the given substrate diffusivity. In essence, a competition instability is an overcrowding instability. Alternatively, as we have shown, the self-replication instability is an undercrowding instability and is triggered when the source parameter of a particular spot exceeds a threshold, or equivalently when there are too few spots in the domain. For a prototypical Schnakenberg model, in [21] it was shown through a center-manifold type calculation that the direction of splitting of a spot is always per-

bioRxiv preprint doi: https://doi.org/10.1101/114876; this version posted March 7, 2017. The copyright holder for this preprint (which was not certified by peer review) is the author/funder. All rights reserved. No reuse allowed without permission.

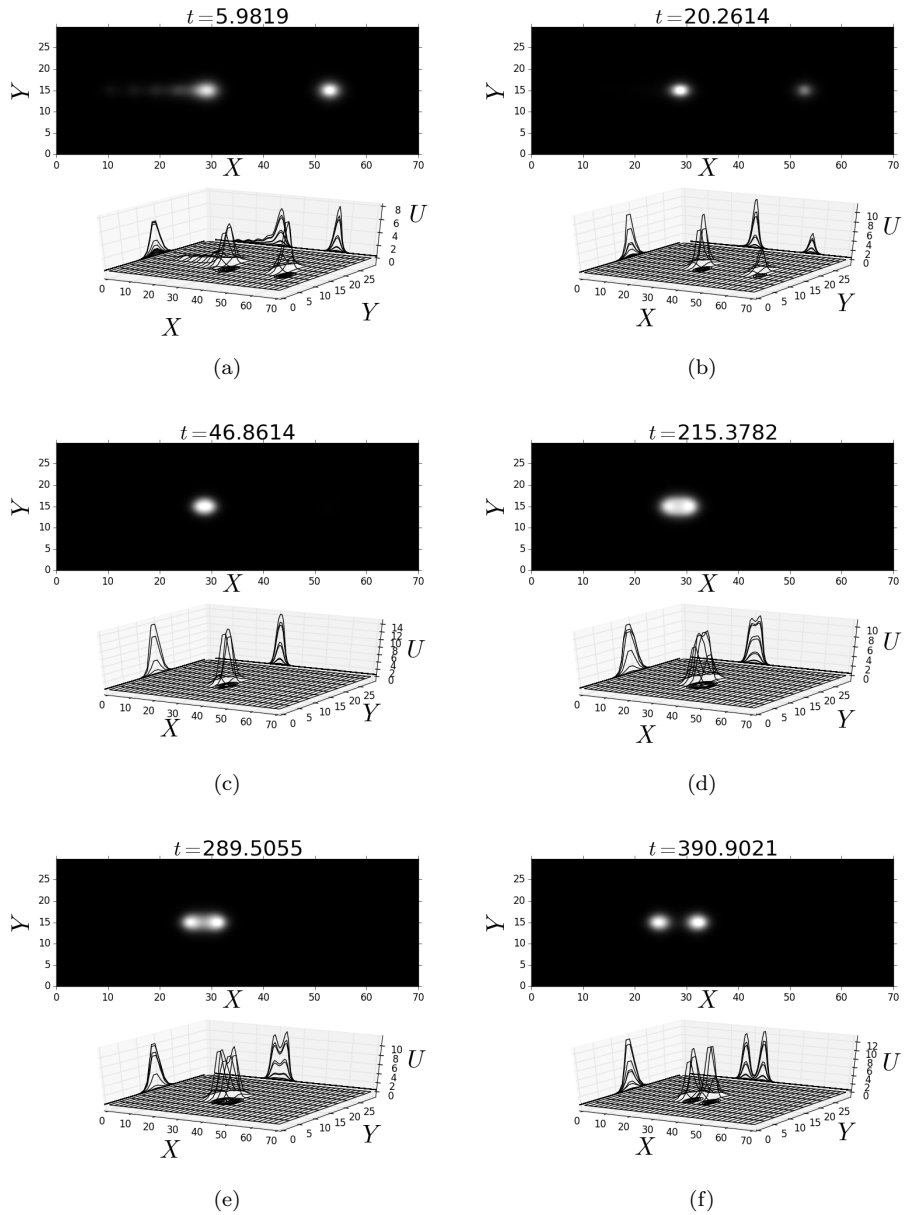

FIG. 10. *Numerical simulations of the full RD system illustrating $\mathcal{O}(1)$ time-scale instabilities. Competition instability: (a) baby droplets and (b) a spot gets annihilated. Spot self-replication: (c) one spot, (d) early stage of a self-replication process, (e) a clearly visible peanut-form, and (f) two distinct spots moving away from each other. Parameter set One as given in Table 1 and* $k_{20} = 1.6133$.

pendicular to the direction of its motion. In our plant RD model, the auxin gradient not only enhances robustness of solutions, which results in the overlapping of solution branches, but it also controls the location of steady-state spots (see subsection 2.2 and section 3). With an auxin gradient the direction of spot-splitting is no longer

bioRxiv preprint doi: https://doi.org/10.1101/114876; this version posted March 7, 2017. The copyright holder for this preprint (which was not certified by peer review) is the author/funder. All rights reserved. No reuse allowed without permission.

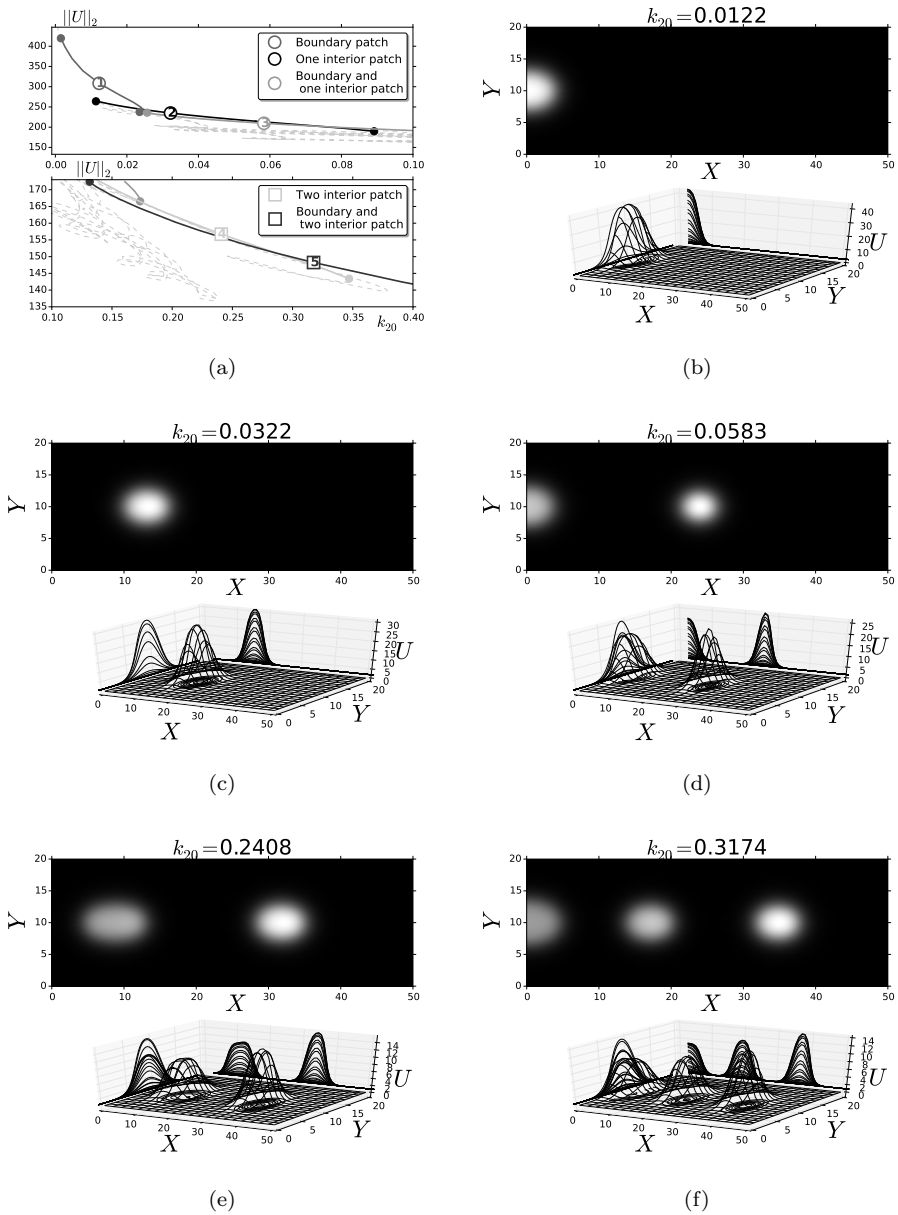

FIG. 11. *Bifurcation diagram of the RD system (1.2) in terms of the original parameters while varying k_{20}. Here $\alpha = \alpha(\mathbf{X})$ as given in (5.41) in a 2-D-rectangular domain. (a) Stable branches are plotted as solid lines, and filled circles represent fold points; top and bottom panels show overlapping of branches of each steady solution: (b) boundary patch, (c) one interior patch, (d) boundary and one interior patch, (e) two interior patches, and (f) boundary and two interior patches. Parameter set Two, as given in Table 1, was used. The k_{20} values are given on top of upper panels for each steady-state in (b)-(f).*

always perpendicular to the direction of motion of the spot.

bioRxiv preprint doi: https://doi.org/10.1101/114876; this version posted March 7, 2017. The copyright holder for this preprint (which was not certified by peer review) is the author/funder. All rights reserved. No reuse allowed without permission.

5. More Robust 2D Patches and Auxin Transport. We now consider a more biologically plausible model for the auxin transport, which initiates the localization of ROP. This model allows for both a longitudinal and transverse spatial dependence of auxin. The original ROP model, derived in [6, 28] and analyzed in [4, 6] and the sections above, depends crucially on the spatial gradient of auxin. The key assumption we have made above was to assume a decreasing auxin distribution along the x-direction. Indeed, such an auxin gradient controls the x-coordinate patch location in such a way that the larger the overall auxin distribution, the more patches are likely to occur. However, as was discussed in section 4, there are instabilities that occur when an extra spatial dimension is present. In other words, when an RH cell is modelled as a two-dimensional flat and thin cell, certain pattern formation attributes become relevant that are not present in a 1-D setting. In particular, 1-D stripes generically break up into localized spots, which are then subject to secondary instabilities depending on the parameter regime. We now want to explore the effect that a 2-D spatial distribution of auxin has on such localized patches of ROP.

5.1. A 2-D Auxin Gradient. In this subsection we perform a numerical bifurcation analysis of the RD system (1.2) in terms of the original parameters and $\tilde{\Omega} \equiv [0, L_x] \times [0, L_y]$, subject to homogeneous Neumann boundary conditions on $\partial\tilde{\Omega}$. We assume an auxin distribution of the form given in (ii) of (1.1),

$$\alpha(\mathbf{X}) = \exp\left(\frac{-\nu X}{L_x}\right)\sin\left(\frac{\pi Y}{L_y}\right) \qquad \text{where} \quad \nu = 1.5\,. \tag{5.41}$$

Such a distribution represents a decreasing concentration of auxin in the X-direction, as is biologically expected, but with a greater longitudinal concentration of auxin along the midline $Y = L_y/2$ of the flat rectangular cell than at the edges near $Y = 0$ and $Y = L_y$.

To perform a numerical bifurcation study we discretize (1.2) using centered finite differences with the auxin distribution as in (5.41), and we adapt the 2-D continuation code written in MATLAB given in [29]. We compute branches of steady-state solutions of this system using pseudo arclength continuation, and the stability of these solutions is computed a posteriori using MATLAB eigenvalue routines. The resulting bifurcation diagram is shown in Figure 11(a). We observe that there are similarities between this bifurcation diagram and the one for the 1-D problem shown in Fig. 6 of [6] in that only fold-point bifurcations were found for the branches depicted. As similar to bifurcation diagrams associated with homoclinic snaking theory on a finite domain (cf. [5, 7, 9, 2, 11]), we observe that all branches seem to lie on a single curve, which consequently gives rise to an overlapping of stable solution branches. With this multistable behavior, hysteretic transitions between solution branches can occur.

To explore fine details of this bifurcation behavior, the bifurcation diagram in Figure 11(a) has been split into two parts, with the top and bottom panels for lower and higher values of k_{20}, respectively. From Figure 11(b) we observe that a boundary patch emerges for very low values of the overall auxin rate. This corresponds to branch 1 of Figure 11(a). As k_{20} is increased to branch 2 of Figure 11(a) there is a single interior patch steady-state, as shown in Figure 11(c). As k_{20} increases further, this interior patch solution persists until stability is lost. Branch 3 in Figure 11(a) consists of stable steady-states of one interior spot and one boundary spot, as shown in Figure 11(d). At even larger values of k_{20}, Figure 11(e) shows that another spot emerges in the interior, corresponding to branch 4 of Figure 11(a). Finally, at much larger values of k_{20}, Figure 11(f) shows that an additional spot is formed at the

bioRxiv preprint doi: https://doi.org/10.1101/114876; this version posted March 7, 2017. The copyright holder for this preprint (which was not certified by peer review) is the author/funder. All rights reserved. No reuse allowed without permission.

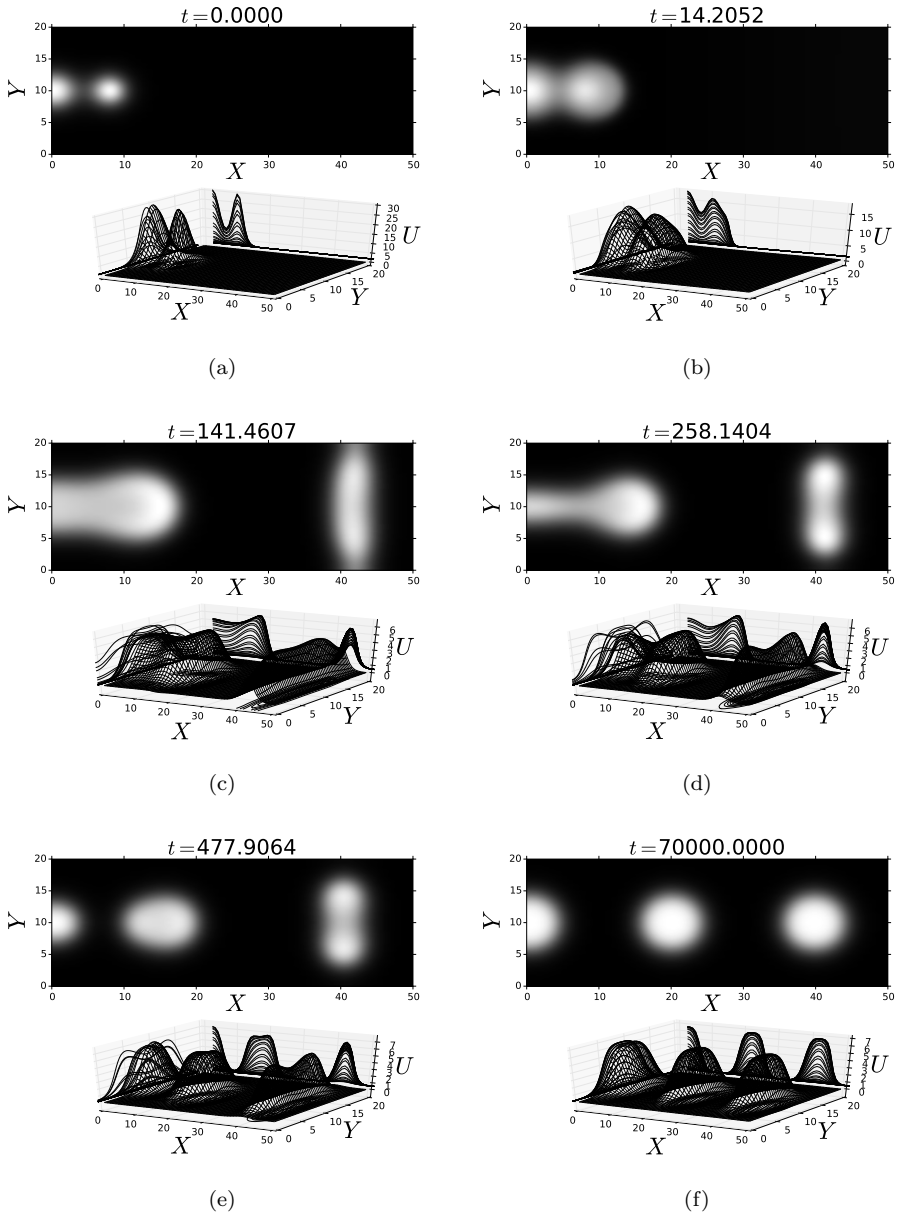

FIG. 12. *Numerical simulations of the full RD system with the 2-D spatial auxin distribution of* (5.41)*. The initial condition, shown in (a), is a boundary and interior patch unstable steady-state. The subsequent time-evolution of this steady-state is: (b) spots merging; (c) a new homoclinic stripe is born; (d) a peanut-form emerges; (e) an interior spot arises from a collapsed peanut-form, and (f) finally, a two interior and one boundary patch stable steady-state. Parameter set Two, as given in Table* 1 *with* $k_{20} = 0.0209$*, was used.*

domain boundary. This qualitative behavior associated with increasing k_{20} continues, and leads to a creation-annihilation cascade similar to that observed for 1-D pulses and stripes in [6] and [4], respectively.

bioRxiv preprint doi: https://doi.org/10.1101/114876; this version posted March 7, 2017. The copyright holder for this preprint (which was not certified by peer review) is the author/funder. All rights reserved. No reuse allowed without permission.

5.2. Instabilities with a 2-D Spatially-Dependent Auxin Gradient. Similarly to the 1-D studies in [4, 6], the auxin gradient controls the location and number of 2-D localized regions of active ROP. As the level of auxin increases in the cell, an increasing number of active ROPs are formed, and their spatial locations are controlled by the spatial gradient of the auxin distribution. Moreover, in analogy with the theory of homoclinic snaking, overlapping of stable solution branches occurs, and this leads to a wide range of different observable steady-states in the RD system.

Transitions from unstable to stable branches are determined through fold bifurcations, and are controlled by $\mathcal{O}(1)$ time-scale instabilities. To illustrate this behavior, we perform a direct numerical simulation of the full RD model (2.6) taking as initial condition an unstable steady-state solution consisting of two rather closely spaced spots, as shown in Figure 12(a). The time-evolution of this initial condition is shown in the different panels of Figure 12. We first observe from Figure 12(b) that these two spots begin to merge at the left domain boundary. As this merging process continues, a new-born stripe emerges near the right-hand boundary, as shown in Figure 12(c). This interior stripe is weakest at the top and bottom boundaries, due to the relatively low levels of auxin in these regions. In Figure 12(d), the interior stripe is observed to give rise to a transversally aligned peanut-form, whilst another peanut-form in the longitudinal direction occurs near the left-hand boundary. The right-most peanut-form is persistent, and leads to a solitary spot, while the left-most form undergoes a breakup instability, yielding two distinct spots, as shown in Figure 12(e). Finally, Figure 12(f) shows a steady-state solution with three localized spots, and no peanut-forms, that are spatially aligned along the Y-midline.

In the instabilities and dynamics described above, the 2-D auxin gradient apparently play a very important role, and leads to ROP activation in the cell primarily where the auxin distribution is higher, rather than at the transversal boundaries. In particular, although a homoclinic-type transverse interior stripe is formed, it quickly collapses near the top and bottom domain boundaries where the auxin gradient is weakest. This leads to a peanut-form centered near the Y-midline, which then does not undergo a self-replication process but instead leads to the merging, or aggregation, of the peanut-form into a solitary spot. The transverse component of the 2-D auxin distribution is essential to this behavior.

We remark that the asymptotic analysis in section 2 and section 3 for the existence and slow dynamics of 2-D quasi steady-state localized spot solutions can also readily be implemented for the 2-D auxin gradient (5.41). The self-replication threshold in subsection 4.1 also applies to a 2-D spatial gradient for auxin. However, for an auxin gradient that depends on both the longitudinal and transverse directions, it is difficult to analytically construct a 1-D quasi steady-state stripe solution such as that done in [6]. As a result, for a 2-D auxin gradient, it is challenging to obtain a dispersion relation predicting the linear stability properties of a homoclinic stripe.

6. Discussion. We have used a combination of asymptotic analysis, numerical bifurcation theory, and full time-dependent simulations of the governing RD system to study localized 2-D patterns of active ROP patches in a two-component RD model for the initiation of RH in the plant cell *Arabidopsis thaliana*. This 2-D study complements our previous analyses in [4, 6] of corresponding 1-D localized patterns. In our RD model, where the 2-D domain is a projection of a 3-D cell membrane and cell wall, as shown in Figure 1, the amount of available plant hormone auxin has been shown to play a key role in both the formation and number of 2-D localized ROP patches observed, while the spatial gradient of the auxin distribution is shown to lead

bioRxiv preprint doi: https://doi.org/10.1101/114876; this version posted March 7, 2017. The copyright holder for this preprint (which was not certified by peer review) is the author/funder. All rights reserved. No reuse allowed without permission.

to the alignment of these patches along the transversal midline of the cell. The interaction between localized active ROP patches and our specific 2-D domain geometry is mediated by the inactive ROP concentration, which has a long range diffusion. This long-range spatial interaction can trigger the formation of localized patches of ROP, which are then bound to the cell membrane.

From a mathematical viewpoint, our hybrid asymptotic-numerical analysis of the existence and slow dynamics of localized active ROP patches, in the absence of any $\mathcal{O}(1)$ time-scale instabilities, extends the previous analyses of [8, 21, 22, 30] of spot patterns for prototypical RD systems by allowing for a spatially-dependent coefficient in the nonlinear kinetics, representing the spatially heterogeneous auxin distribution. In particular, we have derived an explicit DAE system for the slow dynamics of active ROP patches that includes typical Green's interaction terms that appear in other models (cf. [8, 21, 22, 30]), but that now includes a new term in the dynamics associated with the spatial gradient of the auxin distribution. This new term contributing to spot dynamics is shown to lead to a wave-pinning effect whereby localized active ROP patches become aligned along the transverse midline of the RH cell. We have also determined a specific criteria that predicts when an active ROP patch will become linearly unstable to a shape deformation. This criteria, formulated in terms of the source parameter S_j for an individual spot encodes the domain geometry and parameters associated with the inactive ROP density. In addition, the effect of auxin on instability and shape of active-ROP patches is captured by this parameter, and the nonlinear algebraic system for the collection of source parameters encodes the spatial interaction between patches via a Green's matrix. When S_j exceeds a threshold, the predicted linear instability of peanut-splitting type is shown to lead to a nonlinear spot self-replication event.

Although our asymptotic analysis of localized active ROP patches has been developed for an arbitrary spatial distribution of auxin, we have focused our study to two specific, biologically reasonable, forms for the auxin distribution given in (1.1). The first form assumes that the auxin concentration is monotone decreasing in the longitudinal direction, as considered in [6] and [4] and motivated experimentally, with no spatially transverse component. The second form is again monotone decreasing in the longitudinal direction, but allows for a spatially transverse component. This second form is motivated by the fact that our 2-D model is a projection of a 3-D cell membrane and cell wall. As a result, it is biologically plausible that some auxin can diffuse out of the transverse boundaries of our 2-D projected domain, leading to lower auxin levels near the transverse boundaries than along the midline of the cell.

We performed a numerical bifurcation analysis on the full RD model for each of the two specific forms for auxin to determine how the overall level of auxin determines both the number of ROP patches that will appear and the increasing complexity of the spatial pattern. This study showed similar features as in the 1-D studies in [4] in that there are stable solution branches that overlap (see Figure 4(a) and Figure 11(a)), which allows for hysteretic transitions between various 2-D pattern types through fold-point bifurcations. In addition, owing to a homoclinic snaking type structure, a creation-annihilation cascade provides 2-D spatial patterns where both spots, baby droplets, and peanut-forms can occur. Starting from unstable steady-states, our full time-dependent numerical simulations have shown that $\mathcal{O}(1)$ time-scale competition and self-replication instabilities can occur leading to transitions between various spatial patterns. For the auxin distribution model with a transverse spatial dependence, we showed numerically that the active ROP patches are more confined to the transverse midline and that no active ROP homoclinic stripes seem to be possible.

bioRxiv preprint doi: https://doi.org/10.1101/114876; this version posted March 7, 2017. The copyright holder for this preprint (which was not certified by peer review) is the author/funder. All rights reserved. No reuse allowed without permission.

As an extension to our analysis, it would be worthwhile to consider a more realistic domain geometry rather than the projected 2-D geometry considered herein. In particular, it would be interesting to study the effect of transversal curvature on the dynamics and stability of localized active ROP patches. In addition, in [4, 6] and here, transport dynamics of ROPs has been modeled under the assumption of a standard Brownian diffusion process. Even though the experimental observations of pinning in [10, 12, 26] seem to reproduced, at least qualitatively, by our model, it would be interesting to extend our model to account for, possibly, more realistic diffusive processes. In particular, it would be interesting to consider a hyperbolic-type diffusive process having a finite propagation speed for signals, as governed by the Maxwell–Cattaneo transfer law (cf. [25, 36]), or to allow for anomalous diffusion (cf. [16]).

Acknowledgments. D. A., V. F. B.–M. and M. J. W. were supported by EPSRC grant EP/P510993/1 (United Kingdom), UNAM–PAPIIT grant IA104316–RA104316 (Mexico) and NSERC Discovery Grant 81541 (Canada), respectively.

REFERENCES

[1] D. Avitabile, *Numerical computation of coherent structures in spatially-extended systems*. Second International Conference on Mathematical Neuroscience, Antibes Juan-les-Pins, 2016, https://icmns2016.inria.fr/pre-conference-workshop/.

[2] D. Avitabile and H. Schmidt, *Snakes and ladders in an inhomogeneous neural field model*, Physica D: Nonlinear Phenomena, 294 (2015), pp. 24–36.

[3] L. R. Band and J. R. King, *Multiscale modelling of the auxin transport in the plant-root elongation zone*, J. Math. Biol., 65 (2011), pp. 743–785.

[4] V. Brena–Medina, D. Avitabile, A. Champneys, and M. Ward, *Stripe to spot transition in a plant root hair initiation model*, SIAM J. Appl. Math., 75 (2015), pp. 1090–1119.

[5] V. Brena–Medina and A. R. Champneys, *Subcritical Turing bifurcation and the morphogenesis of localized structures*, Phys. Rev. E, 90 (2014), p. 032923.

[6] V. Brena–Medina, A. R. Champneys, C. Grierson, and M. J. Ward, *Mathematical modelling of plant root hair initiation; Dynamics of localized patches*, SIAM J. Appl. Dyn. Sys., 13 (2014), pp. 210–248.

[7] J. Burke and E. Knobloch, *Snakes and ladders: Localized states in the Swift–Hohenberg equation*, Physics Letters A, 360 (2006), pp. 681–688.

[8] X. Chen and M. Kowalczyk, *Dynamics of an interior spike in the Gierer–Meinhardt system*, SIAM J. Math. Anal., 33 (2001), pp. 172–193.

[9] J. Dawes, *Localized pattern formation with a large-scale mode: Slanted snaking*, SIAM J. Appl. Dyn. Sys., 7 (2008), pp. 186–206.

[10] L. Dolan, C. Duckett, C. Grierson, P. Linstead, K. Schneider, E. Lawson, C. Dean, S. Poethig, and K. Roberts, *Clonal relations and patterning in the root epidermis of Arabidopsis*, Development, 120 (1994), pp. 2465–2474.

[11] D. Draelants, D. Avitabile, and W. Vanroose, *Localized auxin peaks in concentration-based transport models of the shoot apical meristem*, Journal of The Royal Society Interface, 12 (2015), pp. 20141407–20141407.

[12] U. Fischer, Y. Ikeda, K. Ljung, O. Serralbo, M. Singh, and R. H. et al., *Vectorial information for Arabidopsis planar polarity is mediated by combined aux1, ein2, and gnom activity.*, Curr. Biol., 16 (2006), pp. 2134–2149.

[13] V. Grieneisen, A. Maree, P. Hogeweg, and B. Scheres, *Auxin transport is sufficient to generate a maximum and gradient guiding root growth*, Nature, 449 (2007), pp. 1008–1013.

[14] C. Grierson and J. Schiefelbein, *The Arabidopsis Book*, American Society of Plant Biologist, 2002.

[15] M. G. Heisler and J. H, *Modeling auxin transport and plant development*, J. Plant Growth Regul, 25 (2006), pp. 302–312.

[16] D. Hernandez, E. C. Herrera-Hernandez, M. Nunez-Lopez, and H. Hernandez-Coronado, *Self–Similar Turing Patterns: An Anomalous Diffusion Consequence*, arXiv:1608.01546, (2016).

[17] A. Jones, E. Kramer, K. Knox, R. Swarup, M. Bennett, C. Lazary, H. O. Leyser, and C. Grierson, *Auxin transport through non-hair cells sustains root-hair development*, Nat.

bioRxiv preprint doi: https://doi.org/10.1101/114876; this version posted March 7, 2017. The copyright holder for this preprint (which was not certified by peer review) is the author/funder. All rights reserved. No reuse allowed without permission.

Cell. Biol., 11 (2009), pp. 78–84.

[18] M. Jones and N. Smirnoff, *Nuclear dynamics during the simultaneous and sustained tip growth of multiple root hairs arising from a single root epidermal cell*, J. of Exp. Bot., 57 (2006), pp. 4269–4275.

[19] M. A. Jones, J. Shen, Y. Fu, H. Li, Z. Yang, and C. Grierson, *The Arabidopsis Rop2 GTPase is a positive regulator of both root hair initiation and tip growth*, The Plant Cell, 14 (2002), pp. 763–776.

[20] T. Kolokolnikov, W. Sun, M. J. Ward, and J. Wei, *The stability of a stripe for the Gierer–Meinhardt model and the effect of saturation*, SIAM J. Appl. Dyn. Sys., 5 (2006), pp. 313–363.

[21] T. Kolokolnikov, M. Ward, and J. Wei, *Spot self-replication and dynamics for the Schnakenberg model in a two-dimensional domain*, J. Nonlinear Sci., 19 (2009), pp. 1–56.

[22] T. Kolokolnikov and M. J. Ward, *Reduced wave Green's functions and their effect on the dynamics of a spike for the Gierer–Meinhardt model*, Europ. J. Appl. Math., 14 (2003), pp. 513–545.

[23] E. M. Kramer, *PIN and AUX/LAX proteins: their role in auxin accumulation*, Trends. Plant Sci., 9 (2004), pp. 578–582.

[24] P. Krupinski, B. Bozorg, A. Larsson, S. Pietra, M. Grebe, and H. Jonsson, *A model analysis of mechanisms for radial microtubular patterns at root hair initiation sites*, Front. Plant Sci., 7:1560 (2016), pp. 1–12.

[25] C. Lattanzio, C. Mascia, R. Plaza, and C. Simeoni, *Analytical and numerical investigation of travelling waves for the Allen–Cahn model with relaxation*, Math. Models Methods Appl., 26 (2016), pp. 931–985.

[26] A. Molendijk, F. Bischoff, C. Rajendrakumar, J. Friml, and M. Braun, *Arabidopsis thaliana ROP GTPases are localized to tips of root hairs and control polar growth*, EMBO J., 20 (2001), pp. 2779–2788.

[27] J. S. Parker, A. C. Cavell, L. Dolan, K. Roberts, and C. Grierson, *Genetic interactions during root hair morphogenesis in Arabidopsis*, Plant Cell, 12 (2000), pp. 1961–1974.

[28] R. Payne and C. Grierson, *A theoretical model for ROP localisation by auxin in Arabidopsis root hair cells*, PLoS ONE, 4 (2009), p. e8337. doi:10.1371/journal.pone.0008337.

[29] J. Rankin, D. Avitabile, J. Baladron, G. Faye, and D. J. B. Lloyd., *Continuation of localised coherent structures in nonlocal neural field equations.*, SIAM J. Sci. Comput., 36 (2014), pp. B70–B93.

[30] I. Rozada, S. Ruuth, and M. J. Ward, *The stability of localized spot patterns for the brusselator on the sphere*, SIAM J. Appl. Dyn. Systems, 13 (2014), pp. 564–627.

[31] M. J. Ward and J. Wei, *Hopf bifurcation and oscillatory instabilities of spike solutions for the one-dimensional Gierer–Meinhardt model*, J. Nonlinear Sci., 13 (2003), pp. 209–264.

[32] J. Wei, *Pattern formations in two-dimensional Gray–Scott model: Existence of single-spot solutions and their stability*, Physica D, 148 (2001), pp. 20–48.

[33] J. Wei and M. Winter, *Spikes for the two-dimensional Gierer–Meinhardt system: The weak coupling case*, J. Nonlinear Sci., 11 (2001), pp. 415–458.

[34] J. Wei and M. Winter, *Spikes for the two-dimensional Gierer–Meinhardt system: the strong coupling case*, J. Nonlinear Sci., 178 (2002), pp. 478–518.

[35] J. Wei and M. Winter, *Stationary multiple spots for reaction-diffusion systems*, J. Math. Biol., 57 (2008), pp. 53–89.

[36] E. P. Zemskov and W. Horsthemke, *Diffusive instabilities in hyperbolic reaction–diffusion equations*, Phys. Rev. E, 93 (2016), p. 032211.